ORIGINAL RESEARCH ARTICLE

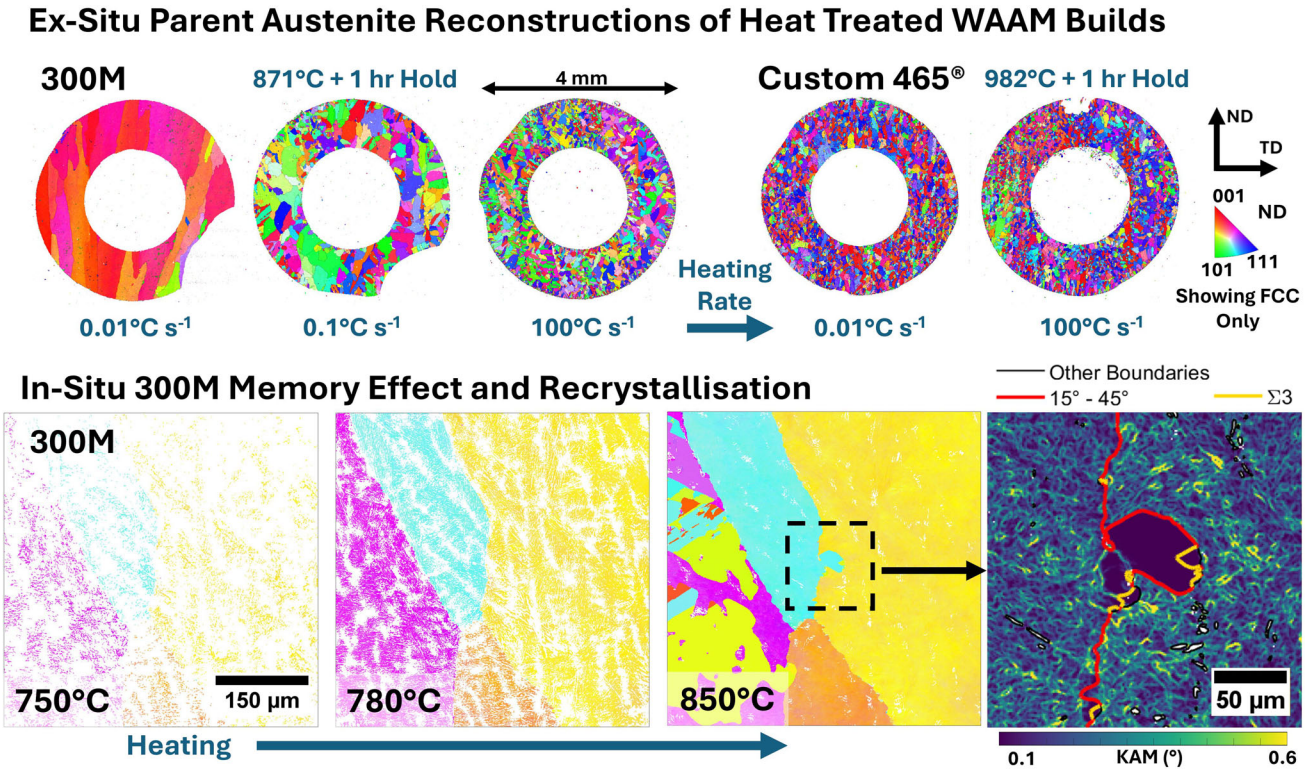
The Effect of Heating Rate and Hold Time on Grain Refinement During the Austenitisation of High-Strength Steels with Coarse Prior Austenite Grain Structures

M. TAYLOR, Y.H. MOZUMDER, A.D. SMITH, J. WANG, Y. LU, S.W. WILLIAMS, F. SCENINI, P.B. PRANGNELL, and E.J. PICKERING

Coarse prior austenite grain (PAG) structures can sometimes be observed in high-strength steels, *e.g.*, in parts produced by wire-arc additive manufacturing (WAAM), and are problematic as they are often associated with poor mechanical performance. In the case of WAAM, cyclic austenitisation can refine coarse PAG structures either during or after the building process. However, in this study we show that there can be a strong effect of heating rate during austenitisation on the resulting grain refinement. The heating rate effect was systematically studied in two steels—a low-alloy steel (300 M) and a maraging steel (Custom 465®)—from an as-WAAM'd state where both comprised coarse columnar PAGs. On heating, for all heating rates investigated and in both steels, the austenite 'memory effect' was first observed, which retained the columnar structure. This was then sometimes followed by autogenous recrystallisation (without applied external deformation), which greatly refined the PAGs. High-temperature *in-situ* electron backscatter diffraction was used to directly observe austenitisation in 300 M, revealing that the recrystallisation shifted from a continuous to a discontinuous mechanism with decreasing heating rate, and that a further decrease in rate suppressed recrystallisation altogether, leaving only a memory effect. Conversely, in Custom 465®, recrystallisation produced significant PAG refinement across all heating rates investigated. However, the recrystallised PAGs retained some crystallographic texture inherited from the columnar PAGs and twins in the as-built material. These findings provide mechanistic insight into grain refinement strategies for steels with coarse PAGs and highlight the importance of controlling heat rates during industrial processing.

M. TAYLOR, Y.H. MOZUMDER, and P.B. PRANGNELL are with the Department of Materials, University of Manchester, Manchester M13 9PL, UK. Contact e-mail: mark.taylor-5@manchester.ac.uk A.D. SMITH is with the TESCAN-UK, Cambridge, UK J. WANG, Y. LU, and S.W. WILLIAMS are with Welding and Additive Manufacturing Centre, Cranfield University, Building 46, Cranfield, Bedfordshire MK43 0AL, UK. F. SCENINI and E.J. PICKERING are with the Department of Materials, University of Manchester and also with the Henry Royce Institute, University of Manchester, Manchester M13 9PL, UK.
Manuscript submitted November 4, 2025; accepted April 22, 2026.

Published online: 25 May 2026



https://doi.org/10.1007/s11661-026-08241-9
© The Author(s) 2026

I. INTRODUCTION

In martensitic and bainitic steels, coarse prior austenite grain (PAG) structures are often associated with poor mechanical properties, which can be exacerbated by the segregation of impurity elements to such boundaries.[1–3] Recently, the development of additive manufacturing has renewed interest in the control of coarse PAG structures through grain refining austenitisation heat treatments.[4,5] This is because, depending on the processing parameters, high-strength steels built using additive manufacturing may develop microstructures composed of coarse columnar PAGs; these structures are prevalent wire-arc additive manufacturing (WAAM) in particular.[6–9] Interestingly, such heat treatments may have limited effectiveness in refining coarse columnar structures if there is a 'memory effect', wherein the PAGs in a martensitic or bainitic steel are reformed during austenitisation.[10–18] This occurs through the growth and coalescence of acicular austenite grains, from the martensitic structure, which are of the same crystallographic orientation as the PAGs that previously occupied the same location.[10–13,15,16,19–28] As a result, the morphology of the original PAGs is reformed upon coalescence, although the dislocation density of these new austenite grains has been found to be higher than that of annealed austenite grains.[14,17,18,29,30] The exact origin of these dislocations is not yet fully understood, although it is very likely to be related to the fact that the memory effect austenite grains maintain an orientation relationship (OR) with the surrounding martensite grains into which they grow. Dislocations may be generated to accommodate the large strains across the transformation interface, caused by the volume mismatch between the two phases.[23,24] Similarly, they may be inherited across the transformation interface from the prior-martensite,[12,15,29] or they could result from an imperfect reproduction of PAG orientation leading to small misorientations between acicular austenite grains upon coalescence.[13] A combination of all three is also a possibility.

In some steels, the dislocation density in the 'memory' austenite grains provides sufficient driving force to cause recrystallisation even in the absence of external deformation, resulting in a new refined austenite grain structure. In certain martensitic steels, this process has been exploited for a long time in the form of cyclic austenitisation treatments,[31,32] but austenite memory effect step has been difficult to observe directly. Both the austenite memory effect and 'autogenous' recrystallisation (also referred to as 'spontaneous' recrystallisation) without the application of external deformation have now been observed by several authors[13–18,28,33] using high temperature *in-situ* EBSD. This has revealed a range of different recrystallisation behaviours across different steel alloys, with some recrystallising through the bulging of pre-existing high angle grain boundaries (HAGB)[33] and others appearing to nucleate new

grains,[13–15,17] and that in some cases the recrystallisation started before austenitisation completed.[14,33] It has been shown that in many alloys increasing the heating rate may produce a finer grain size, and this has been attributed to an increase in the recrystallised grain nuclei.[10–12,17,19,26] However, Rosenauer *et al.*[18] found that heating rate had no effect on the final grain size of PH 13-8 Mo maraging steel post-recrystallisation.

Despite these findings, the extent to which heating rate influences the prevalence of the memory effect and promotes recrystallisation in martensitic steels remains unclear. This work systematically investigated the effect of heating rate on the removal of coarse columnar PAGs in high-strength steel WAAM components during the alloys' respective standard austenitisation heat treatments. The coarse columnar PAG microstructure produced by WAAM provided a distinctive starting microstructure, which allowed PAGs produced by a memory effect or by recrystallisation to be identified post-heat treatment. To provide further insights, the effect of austenitisation hold time and temperature on the resulting grain structure was also briefly assessed. Both 300 M, a medium-carbon steel, and Custom 465® (C465), a maraging stainless steel, were investigated using dilatometry and EBSD. In addition, the austenitisation and recrystallisation of columnar 300 M grains were directly observed with high temperature *in-situ* EBSD. This approach enables a direct comparison of recrystallisation mechanisms across different alloys and thermal conditions, helping to clarify the role of heating rate and hold time in grain refinement.

II. EXPERIMENTAL METHODS

A. *Material Fabrication and Composition*

The 300 M and C465 steels used in this study were fabricated *via* wire-arc additive manufacturing (WAAM) at Cranfield University. The build dimensions and deposition parameters are summarised in Table I. These WAAM builds provided the coarse columnar PAG structures used for subsequent heat treatment and microstructural analysis. The 300 M wall was the same wall used to provide samples in References 33, 34 (referred to as the 'high interpass temperature build' in Reference 34) and has been characterised extensively.

The compositions of the WAAM-produced 300 M and C465 steels are presented in Table II as measured using optical emission spectroscopy (OES) by Element Materials Technology plc.

B. *Dilatometry*

Hollow dilatometry cylinders (4∅ × 10 mm with a 2∅ mm hole) were machined from 300 M and C465 WAAM walls, with the longitudinal direction parallel to the walls' heat-source travel directions (WD), and the circular cross-sections in plane with normal (or build) and transverse directions (ND and TD, respectively), as illustrated in Figure 1. The samples were made hollow (rather than solid) to enable faster heating and cooling as required. A further 2 mm slice with the normal and transverse directions in plane was cut from the 300 M wall and sectioned into 5 × 5 mm^2 samples for *in-situ* EBSD, as also illustrated by Figure 1.

A TA Instruments DIL805 A/D/T dilatometer was used to heat treat the samples according to the illustrative temperature profiles shown in Figures 2(a) and (b), and the full dilatometer heat treatment matrix is summarised in Table III. Samples were heated under

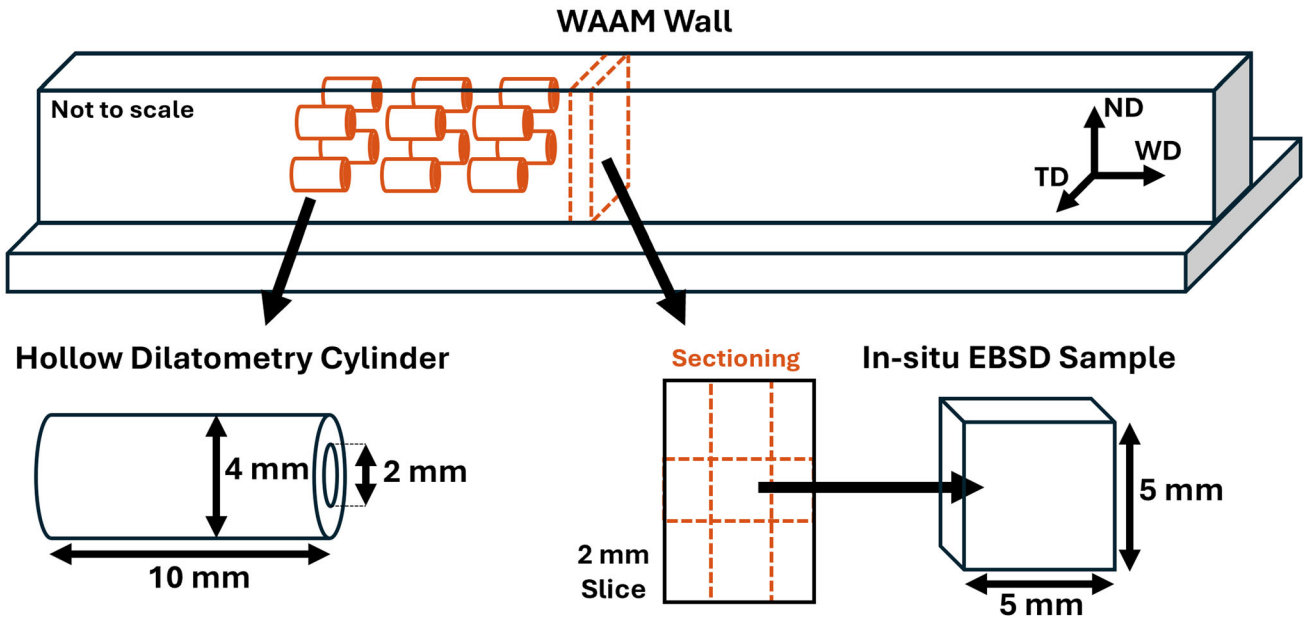


Fig. 1—A schematic displaying how the dilatometer and *in-situ* EBSD samples were machined from the WAAM walls.

Table I. WAAM Parameter Used to Build the 300 M and C465 Walls

Material and Dimensions (Height × Width × Length mm^3)	Wire Feeding Speed (m min^{-1})	Torch Travel Speed (mm s^{-1})	Deposition Current (A)	Gas Flow-rate (L min^{-1})	Shielding Condition	Interpass Temp.
300 M 22 × 12 × 270	2.35	3.3	210	0.8	Ar global O < 500 ppm	continuous deposition
C465 105 × 12 × 250	2.35	3.3	210	85	Ar global O < 500 ppm	~ 100 °C

Table II. Composition of the 300 M and C465 Used in this Study as Measured Using OES

Material	C	Cr	Mn	Mo	Ni	P	S	Si	V	Ti
300 M	0.42	0.85	0.80	0.38	1.76	0.006	0.008	1.66	0.08	< 0.01
C465	< 0.01	11.4	< 0.01	0.95	11.0	< 0.005	< 0.003	0.08	—	1.57

vacuum to their respective austenitisation/solution treatment temperatures (871 °C for 300 M[35] and 982 °C for C465[36,37]) at rates ranging from 100 °C s^{-1} to 0.01 °C s^{-1}, and then held for 1 hour before being quenched to room temperature in Ar at 10 °C s^{-1} to produce a martensitic microstructure and prevent grain growth during cooling. Gas was blown through the centre of the tubes to achieve this cooling rate. For both alloys, two samples were heated at 100 °C s^{-1} and 0.1 °C s^{-1}, respectively, and immediately quenched without a hold at peak temperature. This was done to examine the effect of holding time on recrystallisation. Another two samples (again at 100 °C s^{-1} and 0.1 °C s^{-1}) were heated to intermediate temperatures just above the austenitisation finish temperature (Ac_3), but below the standard austenitisation temperature—840 °C for 300 M and 750 °C for C465—and held for 1 hour before quenching. These tests aimed to evaluate the influence of proximity to Ac_3 on recrystallisation. Finally, two extra 300 M samples were heated to 700 °C following the 0.01 °C s^{-1} temperature profile, then rapidly heated to 871 °C following the 100 °C s^{-1} profile (referred to as 0.01 → 100 °C s^{-1} profile) as illustrated in Figure 2(b). The first was held at 871 °C for 1 hour and then quenched, this test was designed to determine whether the heating rate *prior* to austenitisation (rather than *through* austenitisation) affects recrystallisation behaviour. The second was immediately quenched from 871 °C, it was used to compare the carbide distributions created by the 0.01 → 100 °C s^{-1} heating profile, with those created in the sample heated to 871 °C at the 100 °C s^{-1} heating rate only and then immediately quenched. For 300 M, a 1 hr hold at 871 °C would likely dissolve most carbides formed during heating, therefore it was necessary to use samples that had been quenched immediately after heating. The three immediately quenched samples used to compare carbide distributions are highlighted in bold in Table III.

All dilatometry samples were sectioned in half (circular cross-section), polished to a 0.04 μm OPS finish and EBSD mapped using a ThermoScientific Apreo SEM equipped with an Oxford Instrument Symmetry 2 EBSD detector, using a step size of 1 μm an accelerating voltage of 20 kV and a current of ~ 51 nA. Afterwards, frames were stitched together using AZtec 6.1 software and PAGs reconstructed using AZtec Crystal 3.1 software. EBSD maps were also recorded from both steels in the as built state to provide a before and after comparison. Finally, to aid identification of micro-constituents and carbides, the as-built 300 M sample and the 300 M samples marked in bold in Table III were etched using 2 pct nital. The as-built material was imaged using an optical microscope, whilst carbides in the two dilatometry samples were imaged using a FEI Magellan 400 in secondary electron (SE) mode with an accelerating voltage of 20 kV and current of 0.4 nA.

C. *In-situ EBSD*

Two *in-situ* high temperature EBSD experiments were performed using a TESCAN and NewTec *In-situ* Testing rig (TANIST). This setup included a TESCAN Clara with a Newtec FurnaSEM 1000 heating stage, an Oxford Instruments Symmetry 3 EBSD detector, and an UltimMax 170 mm EDS detector. The FurnaSEM software interfaced with the microscope and detector software allowing for automated heating, focussing, brightness/contrast, region tracking, SE and EBSD imaging according to a pre-determined program.[38] The temperature was held constant during region tracking and imaging stages, thus the overall heating rate achieved was in part determined by the time taken to collect an image or EBSD map. It should be noted that temperature was measured using a thermocouple in the base of the heating stage. Therefore, there may have been a temperature difference of up to 20 °C (although it may be much less) between this thermocouple and the sample surface imaged; the implications of this gradient are discussed in detail in the relevant section.

The temperature profiles are shown in Figure 2(b). In both tests, only SE images were collected during heating to a temperature of interest, before the heating rate was reduced as EBSD mapping commenced. In Test 1, the

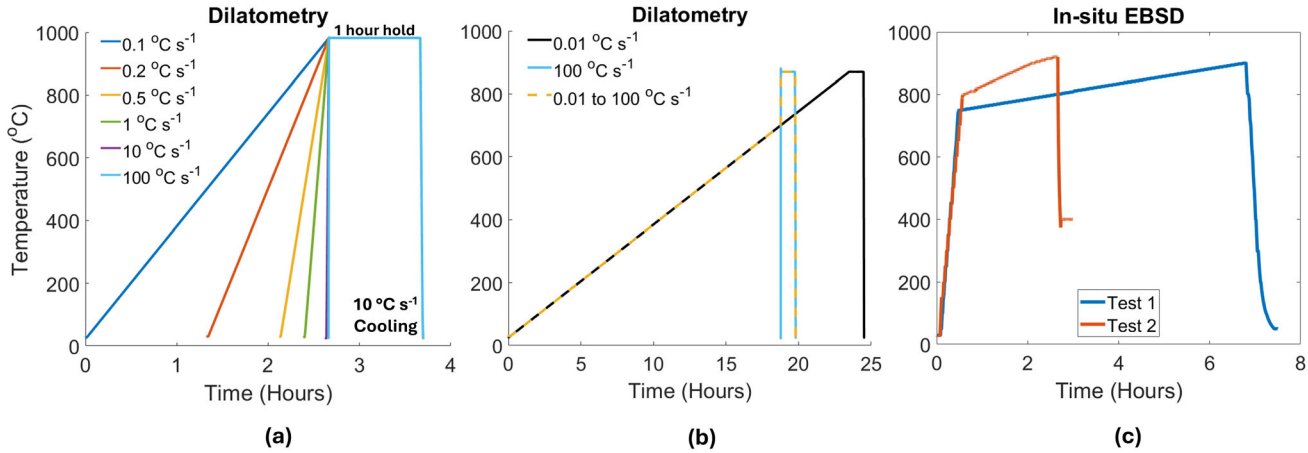


Fig. 2—(*a*) and (*b*) Example temperature profiles used for the dilatometry experiments with holds. Samples were heated to their respective austenitisation temperature (871 °C for 300 M and 982 °C for C465) with one of 6 different heating rates. The yellow dashed profile was performed for 300 M only. (*c*) The temperature profiles used for the two 300 M *in-situ* EBSD experiments (Color figure online).

Table III. Dilatometer Heat Treatment Matrix. Bold Font Indicates Samples Etched for Secondary Electron Imaging of Carbides

Test Matrix X = Test Performed		Heating Rate (°C s^{-1})							
		0.01	0.1	0.2	0.5	1	10	100	0.01 → 100
300 M	871 °C 1 hour hold	×	×	×	×	×	×	×	×
	871 °C no hold		**×**					**×**	**×**
	840 °C 1 hour hold		×					×	
C465	982 °C 1 hour hold	×	×	×	×	×	×	×	
	982 °C no hold		×					×	
	750 °C 1 hour hold		×					×	

sample was automatically heated to 750 °C with SE region tracking before EBSD maps (500 μm field width, 0.7 μm step size) were then collected every 2 °C with a 1 °C s^{-1} heating rate in-between. After heating to 900 °C the sample was cooled to room temperature. Test 2 was designed to allow less time for recovery processes by using a faster heating rate during the EBSD mapping segment. It followed the same automated temperature program as Test 1 until 750 °C. Unlike in Test 1, in Test 2 faster EBSD maps (700 μm field width, 2 μm step size) were collected more frequently (every 5 °C with a 1 °C s^{-1} heating rate in-between), starting from the higher temperature of 800 °C. For Test 2, cooling to room temperature commenced from 920 °C as recrystallisation had not completed by 900 °C. For Test 1 *in-situ* EBSD, a 30 kV accelerating voltage and ~ 30 nA current were used to enable fast indexing, and for Test 2 a 20 kV accelerating voltage and ~ 30 nA were used. All EBSD parameters and beam conditions were kept the same throughout heating (although exposure time was increased for the room temperature maps as discussed below). The datasets were analysed using scripts written using the MTEX 5.10.2 toolbox.[39] Further details regarding the alloy EBSD parameters, PAG reconstruction parameters, and *in-situ* rig can be found by following the link in Reference 40.

Before both tests, a room temperature EBSD map with simultaneous EDS was collected. The exposure time was increased for these pre-heating maps to increase the EDS signal. The PAGs were reconstructed from these EBSD maps with the MTEX 5.10.2 variant graph approach[41,42] and the reconstruction used to confirm whether a memory effect had occurred or not at high temperature. Similarly, the EDS map was used to confirm the presence of compositional microsegregation. During each PAG reconstruction, the OR between martensite and austenite was calculated using an MTEX algorithm described in reference.[43] It iteratively refined the OR for this material using the Kurjumov–Sachs (K–S) OR. The final refined OR was less than 2.5 deg away from the K–S OR for both tests. This OR was used for the PAG reconstruction and for further analysis of the whole dataset, as will be discussed later.

III. RESULTS

In this section, 300 M and C465 results are presented separately to avoid confusing their separate austenitisation and recrystallisation behaviours. For both steels, the pre-heat-treatment as-built microstructures are presented first, followed by post-heat treatment EBSD

PAG reconstructions, and finally the dilatometry curves measured during those heat treatments. For 300 M only, *in-situ* EBSD is also presented.

A. *As-Built Microstructure of 300 M*

The as-built microstructure of the 300 M build consisted of predominantly martensite with some bainite, as shown by the optical micrographs in Figures 3(a) and (b). It contained pronounced compositional microsegregation typical of WAAM'd alloys,[6,9] resulting from the segregation of alloying elements to the interdendritic/dendritic regions during initial solidification from the melt pool. In 300 M, Si, Cr, Mn, Mo and Ni have all been reported[6,44] to enrich the interdendritic regions (partition coefficient is $k < 1$), including in references,[33,34] which used samples from the same build. When etched in nital, the interdendritic regions appeared lighter, as can be seen in Figure 3(a) and the higher magnification image depicted in Figure 3(b) demonstrates that these lighter etching regions were not related to the martensite grain structure, as both sheaves and laths can be seen to cross them. Additionally, Reference 34 demonstrated that the microsegregation is also not directly related to the PAG structure as it exists on a much smaller length scale.

Figure 3(c) displays an EBSD PAG reconstruction of the as-built 300 M microstructure, it was constructed from a larger EBSD map published in Reference 34. As expected, the microstructure contains large columnar PAGs with both the long dimension and the crystallographic ⟨001⟩ poles often aligned to the normal direction, as evidenced by the predominance of red coloured columnar grains in the orientation map (IPF colours defined by alignment to the build ND). The PAG size has not been given since they were longer than the dimensions of the area mapped (4 mm). It should be noted that a minority fraction of PAGs with other orientations were also present [see the non-red grains in Figure 3(c)].

B. *Austenitisation Behaviour of the 300 M Dilatometry Samples*

The distinctive PAG structure of the as-built material [Figure 3(c)] made it easy to determine whether the dilatometry heat treatments had produced a memory effect only, or recrystallisation of the memory orientation austenite grains. Examples where a memory effect and no recrystallisation was observed are shown in Figure 3(d). Here, the slow and fast heating rate samples that were heated to 871 °C and immediate quench (not held at temperature) possess a very similar PAG structure to that of the as-built material in (c), despite having undergone austenitisation (evidence shown in section III–C).

Evidence of recrystallisation was easily recognised by a refinement in grain size and a loss of the strong ⟨001⟩ fibre texture. This can be seen in Figure 4(a), which displays the PAG reconstructions of the 300 M samples conventionally austenitised at 871 °C for 1 hour, after heating from room temperature at rates from 0.01 °C s^{-1} and 100 °C s^{-1}. The slowest heating rate of 0.01 °C s^{-1} supressed recrystallisation entirely, leaving only a memory effect, whilst increasing the heating rate between 0.1 °C s^{-1} and 100 °C s^{-1} led to more grain refinement (244 μm area weighted equivalent circle diameter for 0.1 °C s^{-1} to 111 μm for 100 °C s^{-1}), although recrystallisation occurred in all cases. The 0.5 °C s^{-1}, 1 °C s^{-1} and 10 °C s^{-1} heating rate samples are not displayed in Figure 4(a) to save space, but had refined PAG structures very similar to the 100 °C s^{-1} sample (0.5, 1, and 10 °C s^{-1} had 110, 95 and 77 μm PAG diameters, respectively). Interestingly, for the 300 M samples that were held at the lower austenitisation temperature of 840 °C for 1 hour [Figure 4(b)] to investigate the influence of proximity to Ac_3 on recrystallisation, the 0.1 °C s^{-1} heating rate sample displayed only a memory effect, whilst the 100 °C s^{-1} heating rate sample recrystallised. These results highlight that recrystallisation in 300 M can be promoted by rapid heating whereas slower heating tends to preserve the memory effect.

The two stage 0.01 → 100 °C s^{-1} profile to 871 °C was designed to investigate whether the heating rate *prior* to austenitisation (rather than *through* austenitisation) affects recrystallisation behaviour. EBSD PAG reconstructions of the samples heated using this profile are displayed in Figure 5, here the IPF colour key was aligned to the welding direction to better highlight recrystallised grains. Partial recrystallisation was observed in both samples regardless of whether they were then held for 1 hour or immediately quenched, (a) and (b), respectively. Non-memory orientation PAGs were distributed throughout strongly textured large columnar memory effect PAGs, indicating that although recrystallisation started it, the recrystallised grains were not able to completely consume non-memory grains before the sample was quenched. In the sample that was held at temperature for 1 hour [Figure 5(a)] the non-memory orientation grains were slightly larger than in the sample that was not [Figure 5(b)], indicating that recrystallisation had progressed further during the hold , although it did not reach completion.

Figure 6 compares the etched microstructures of the three 300 M dilatometry samples that were heated to 871 °C and then immediately quenched. The sample in (a) was heated with the two stage 0.01 → 100 °C s^{-1} profile, and the samples in (b) and (c) were with constant heating rates of 100 °C s^{-1} and 0.1 °C s^{-1}, respectively. Although all three microstructures were martensitic, the 0.01 → 100 °C s^{-1} heating profile clearly produced a distribution of coarse particles, that were not present in the constant heating rate samples in (b) and (c), or any samples held at 871 °C for 1 hour (supplementary SE images provided in Reference 40). These particles were assumed to be carbides since (1) they are well known to form in 300 M,[1,3,4,45] (2) supplementary EDS data provided in Reference 40 shows them to be enriched in Cr and C and (3) the dilatometry data presented in the next section displays evidence of carbide formation. Comparatively refined particles, also assumed to be carbides, were concentrated in the compositionally enriched (interdendritic) regions of the sample heated

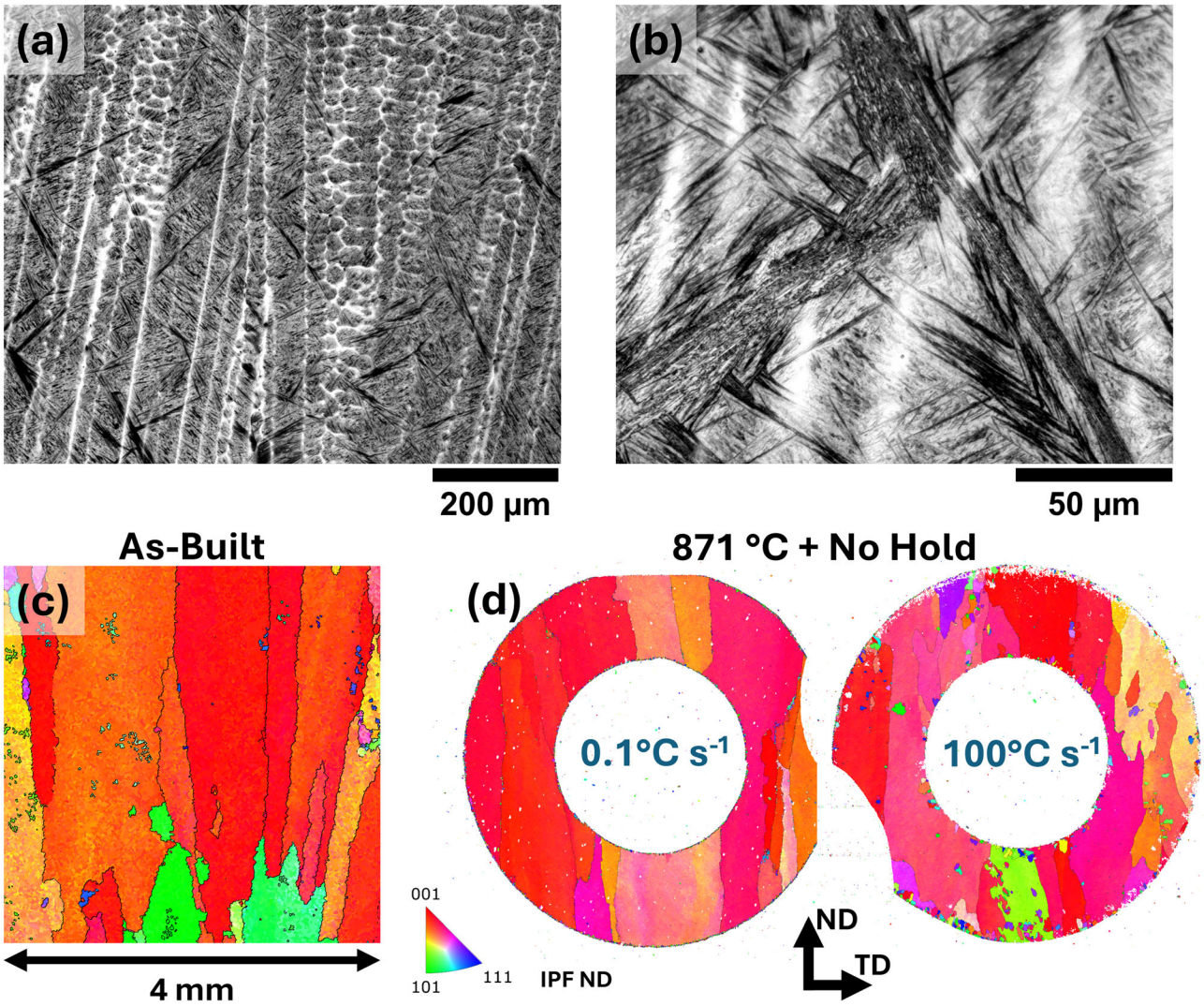


Fig. 3—(*a*) and (*b*) Optical micrographs of the 300 M wall in the as-built condition after nital etching, at (a) low magnification and (b) higher magnification. (*c*) An EBSD PAG reconstruction of the as-built 300 M microstructure. (*d*) EBSD PAG reconstructions of the 300 M dilatometry sample cross-sections heated to 871 °C and immediately quenched, at slow and fast heating rates, respectively.

at 0.1 °C s^{-1} and immediately quenched [Figure 6(c)]. Supplementary EDS and lower magnification SE images have been provided in Reference 40 to demonstrate that these refined carbides were both enriched in Mo and located in interdendritic regions, and also that they were sometimes present in the samples held at 871 °C for 1 hour.

C. *Austenitisation Dilatometry Measurements of 300 M*

Figure 7(a) displays the dilatometry curve measured during the conventional 871 °C 300 M heat treatment using a heating rate of 0.1 °C s^{-1}, the shape of this curve typified that measured during all the 300 M dilatometry tests. The temperature range between 300 °C and 871 °C, where there are two de*via*tions from linear thermal expansion during heating, has been magnified in Figure 7(b) and the other heating rates investigated have been plotted offset from the 0.1 °C s^{-1} curve. It can be seen that all 300 M samples were austenitised by 871 °C, and that increasing heating rate increased the austenite start (Ac_1) and finish (Ac_3) temperatures [see markers on Figure 7(b)], as expected.[30] Based on these curves, it would appear that the sample heated to 840 °C at 100 °C s^{-1} would not have fully austenitised. However, the 840 °C samples were subsequently held for an hour above the Ac_3 temperature measured for slower heating rates and therefore had ample time to austenitise. It should be noted that during the most rapid 100 °C s^{-1} heating rate treatments the temperature overshot the target peak temperature by up to 10 °C, whilst the target peak temperature was achieved to an accuracy of ± 1 °C for all other tests. The 9 °C overshoot found in the fast-heating rate 840 °C test was not believed to have affected the results significantly since 849 °C still represents a temperature between the Ac_3 temperature and the conventional austenitisation temperature of 871 °C.

300 M contained an additional contraction prior to austenitisation, which is highlighted in both Figures 7(a) and (b). In the literature,[45] this has been associated

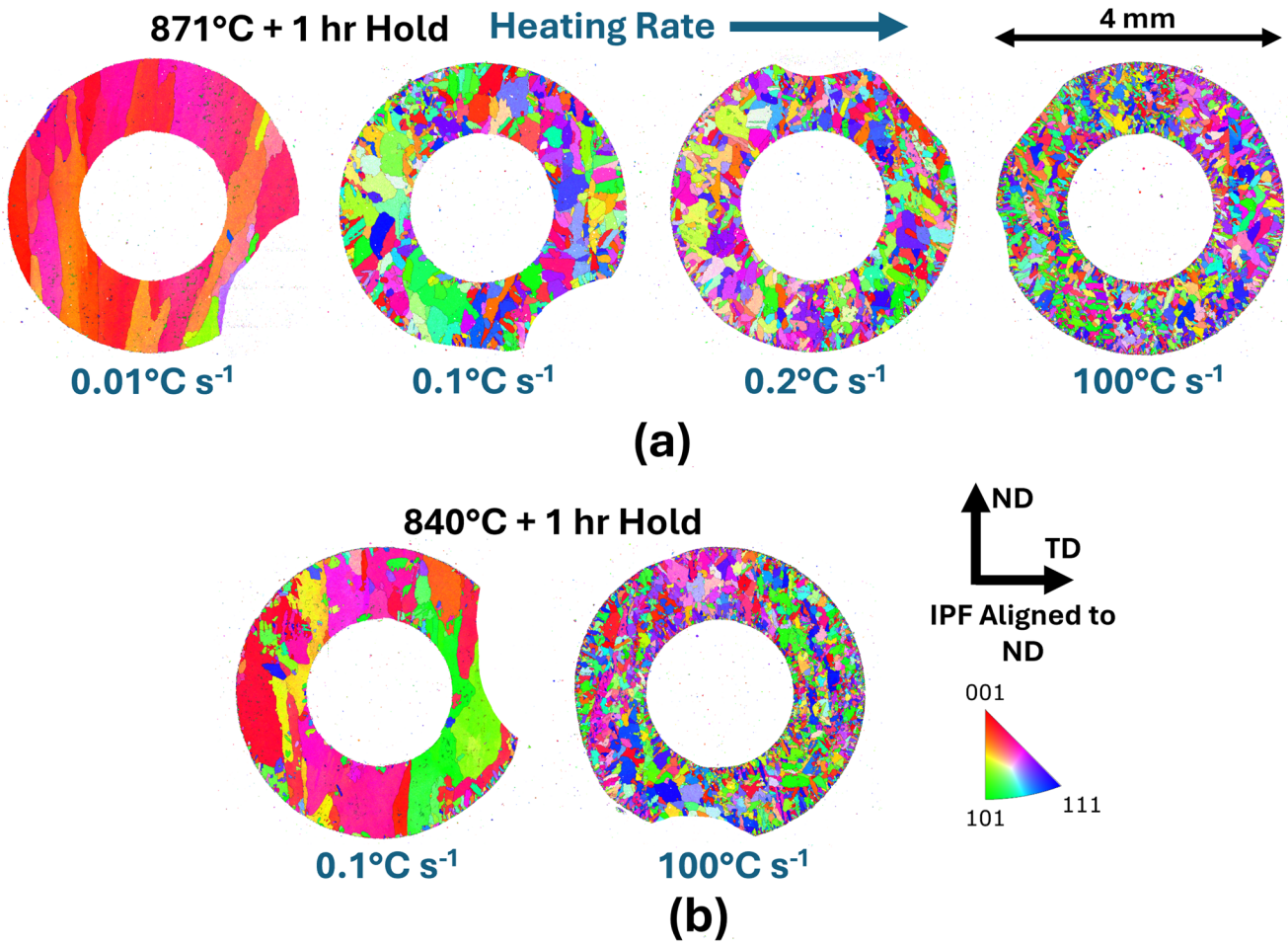


Fig. 4—EBSD PAG reconstructions from the 300 M dilatometry investigation. (*a*) The 871 °C and 1 h hold samples with varying heating rates. (*b*) The samples heated to the lower 840 °C austenitisation temperature and held for 1 h with slow and fast heating rates.

with the precipitation and growth of carbides in 300 M. In Figure 7(b), the contraction can be seen to drift to higher temperatures with increasing heating rate. Another contraction can be seen in some curves at approximately 740 °C at the start of austenitisation, this is thought to be associated with magnetic effects related to heating with an induction coil.[46]

D. *In-situ Experiments on 300 M*

To investigate the effect of recovery time after Ac_1 on the recrystallisation mechanism, two *in-situ* EBSD experiments were performed: Test 1 with slower heating and more time for recovery, and Test 2 with faster heating and reduced recovery time. Figure 8 displays the EBSD, PAG reconstructions and simultaneous EDS maps for both Test 1 (a) through (c) and 2 (d) through (f), prior to conducting the *in-situ* experiments. The PAG reconstruction in Figure 8(b) shows that the area selected in Test 1 covered an intersection between four columnar grains with no common orientation between them. In comparison, Test 2 covered an area containing two large columnar PAGs, both with a strong ⟨001⟩ alignment to the build normal direction as shown by the reconstruction in Figure 8(e).

The EDS maps for the sample areas imaged in Tests 1 and 2, displayed in Figures 8(c) and (f), respectively, were acquired from the exact same regions as the corresponding EBSD maps to enable direct correlation between microstructure and composition. It should be noted that EDS signal was weak due to the sub-optimal conditions for EDS (longer working distance and tilted), especially in Figure 8(f). However, Si intensity maps were still sufficient to reveal the location and morphology of the microsegregation. Other elements also segregate, but this map was only intended to reveal the location of alloying element enriched microsegregation. The precise alloying elements which segregate in during WAAM of 300 M have been reported previously.[6,33]

Figures 9(a) and (b) displays SE images collected from the exact same region as shown in the Figures 8(a) through (c) maps, during heating stages of Test 1 at 352 °C and 864 °C, respectively. They demonstrate how particles that appear bright in SE imaging mode, nucleate and coarsen in the interdendritic compositionally enriched regions first during heating. A compositionally enriched region from these images has been magnified in Figure 9(c), to highlight how the particles concentrate and coarsen within this region. The shallow dimples seen on the surface of (a) were related to slight

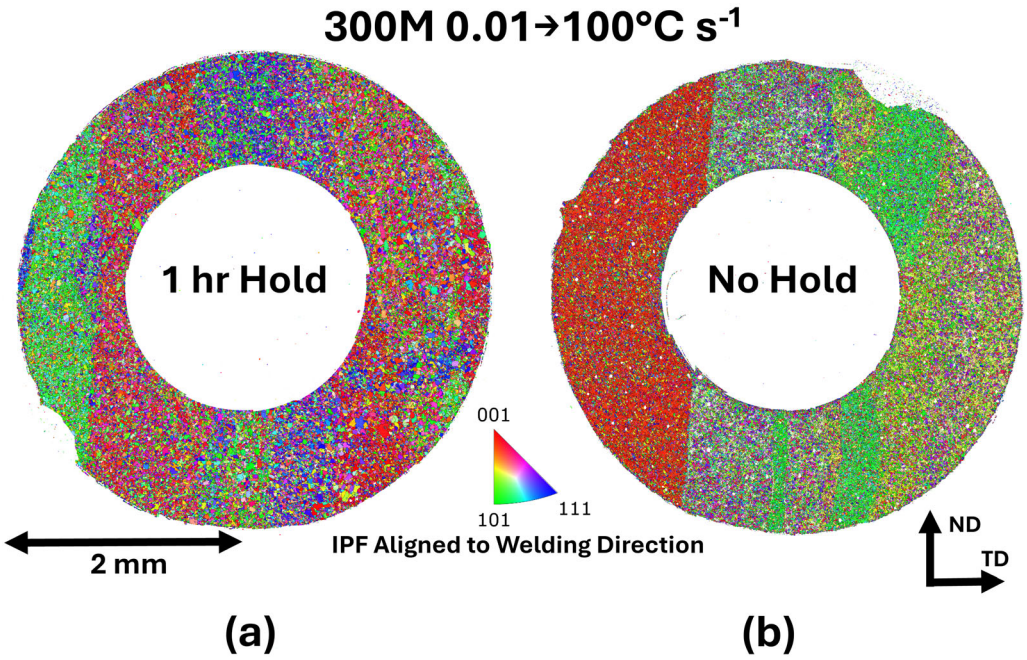


Fig. 5—The samples heated to 871 °C with the 0.01 → 100 °C s^{-1} heating profile, (*a*) was held for 1 h hold before quenching and (*b*) was immediately quenched after reaching 871 °C. The IPF key here was aligned to the welding (torch travel) direction as these colours better highlight the small grains present within larger columnar grains (Color figure online).

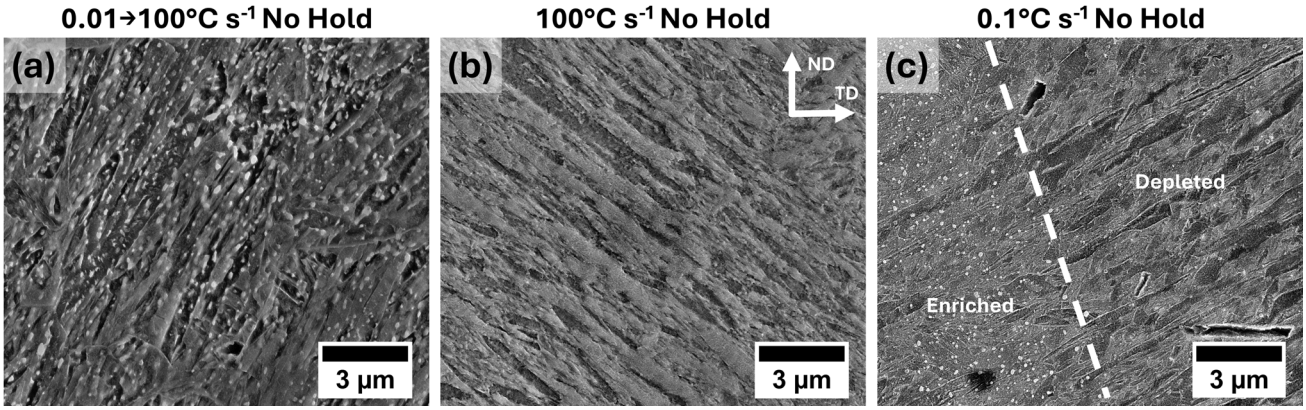


Fig. 6—SE images from etched 300 M dilatometry samples (bold in Table III) heated to 871 °C (*a*) using the 0.01 → 100 °C s^{-1} heating profile (*b*) at 100 °C s^{-1} and (*c*) at 0.1 °C s^{-1}. All three samples were immediately quenched after reaching 871 °C.

uneven BIB polishing around carbides or inclusions. They were not removed as they aided region tracking and did not affect EBSD mapping.

Animated GIFs ('videos') created using the images from both *in-situ* experiments can be found by following the link in Reference 47. The MATLAB scripts used for the analysis, all images and the raw data can be found by following the link in Reference 40. Figures 10 and 11 display four select EBSD frames from heating during the Test 1 and 2 *in-situ* experiments on 300 M, respectively. In both figures, the same frames are displayed as phase colour maps in (a), FCC phase orientation maps in (b) and kernel average misorientation (KAM) maps with high angle and twin boundaries highlighted by red and gold, respectively in (c). An area from the Test 1 850 °C frame and from the Test 2 900 °C frame, have been magnified in Figure 12 to enable easier viewing of key features. In both experiments, 300 M first displayed a memory effect as described in other steels in the literature[13–18,28,33] and recrystallised autogenously upon further heating, *i.e.*, without the application of external deformation. The memory effect proceeded *via* the nucleation of acicular austenite grains, with the memory orientation, at martensite lath boundaries. These grains eventually coalesced into austenite grains with the same orientation and morphology as the PAGs. This can be seen by comparing the FCC orientation maps in Figures 10(b) and 11(b) with their corresponding pre-heating PAG reconstructions in Figures 8(b) and (e). However, KAM maps in Figures 10(c) and 11(c) revealed that these grains contain considerable internal misorientation, indicative of high dislocation density

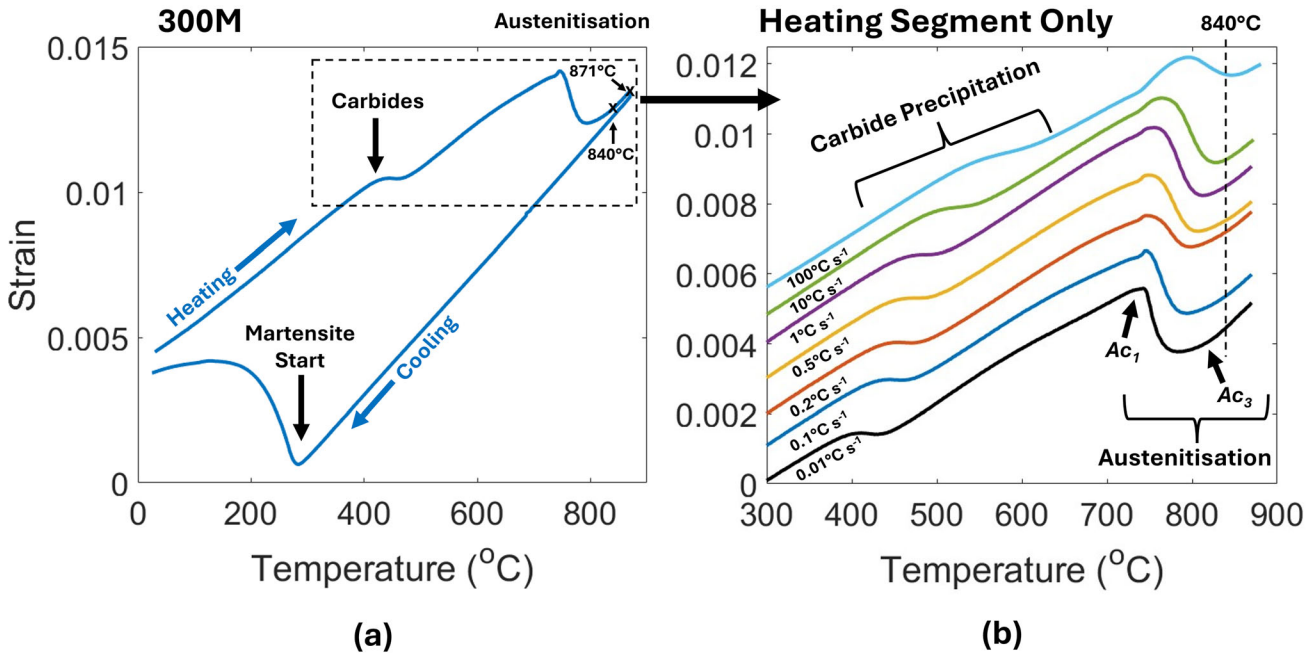


Fig. 7—(*a*) The full dilatometry curve from the 300 M 0.1 °C s^{-1} heating rate to 871 °C test, with a 1 h hold at temperature. (*b*) The heating data between 300 °C and 870 °C from the boxed section shown in (a). The same region from the other the 300 M dilatometry curves with different heating rates are also displayed, their strain has been offset to allow for direct comparison.

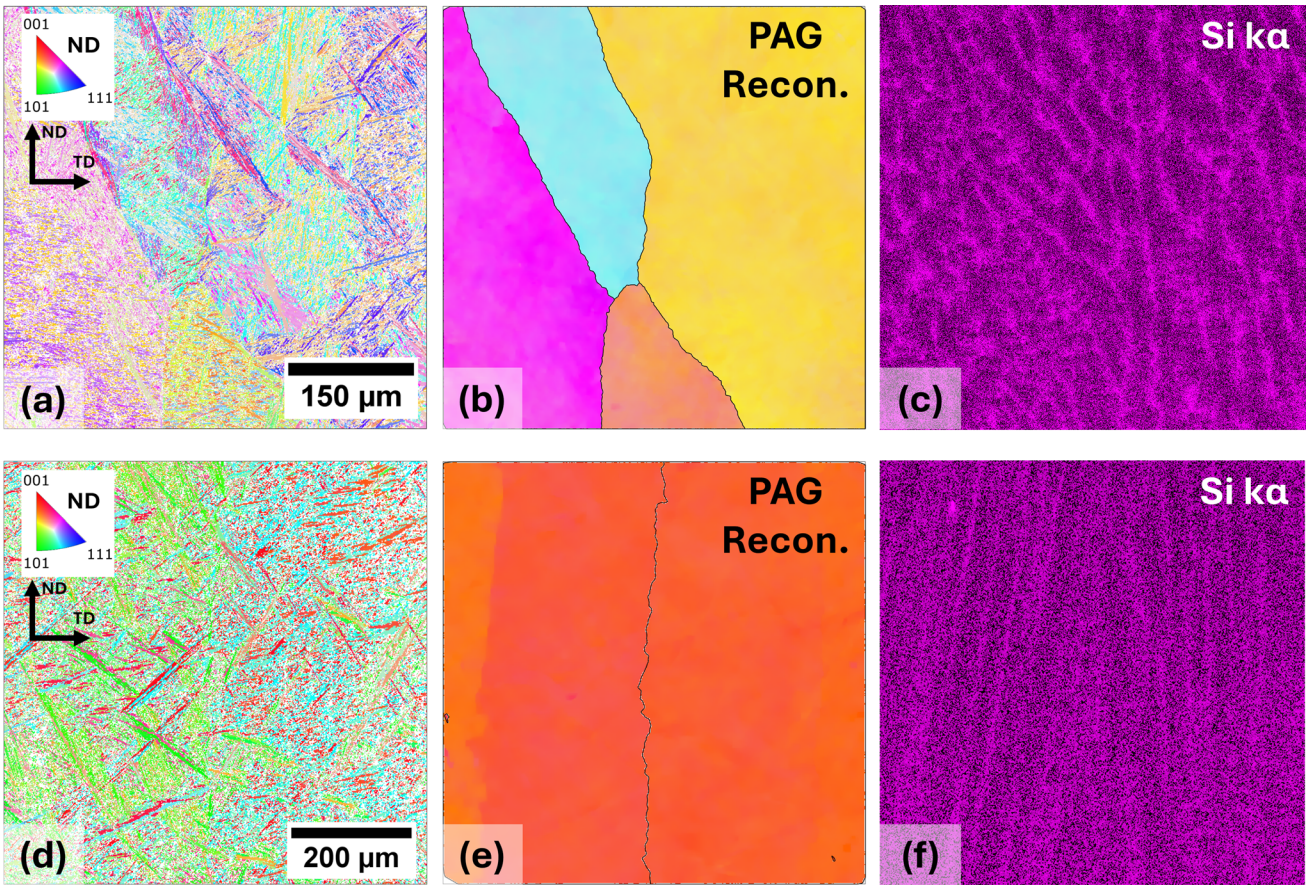


Fig. 8—(*a*) through (*c*) EBSD orientation map of the Test 1 300 M *in-situ* experiment region prior to heating, its PAG reconstruction with grain boundaries shown in black (> 10 deg), and a kα intensity Si EDS map collected simultaneously. (*d*) through (*f*) Equivalent maps for Test 2 (Color figure online).

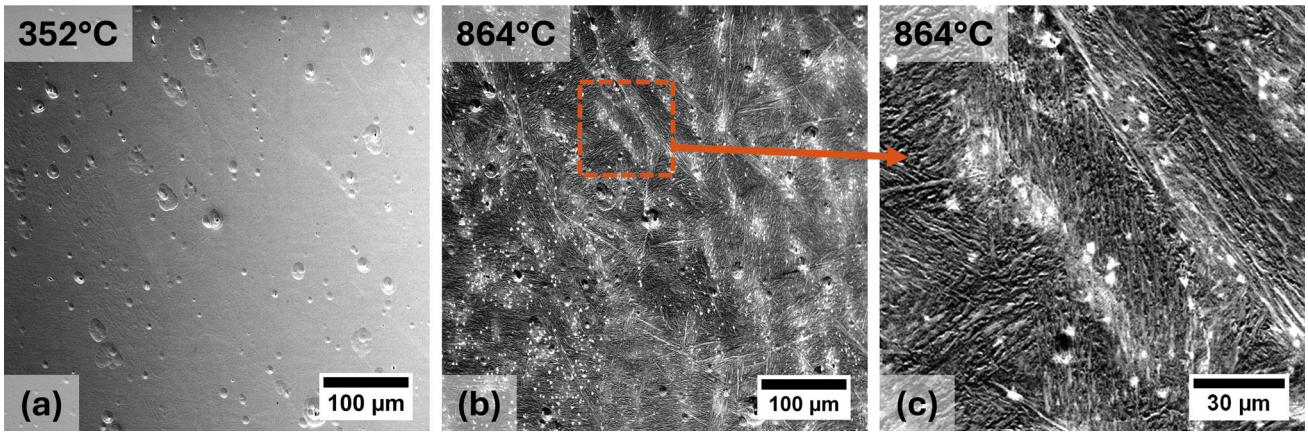


Fig. 9—(*a*) and (*b*) SE images of the Test 1 *in-situ* EBSD region at 352 °C and 864 °C, respectively, showing particle evolution in enriched areas. (*c*) Magnified view of the boxed region in (b).

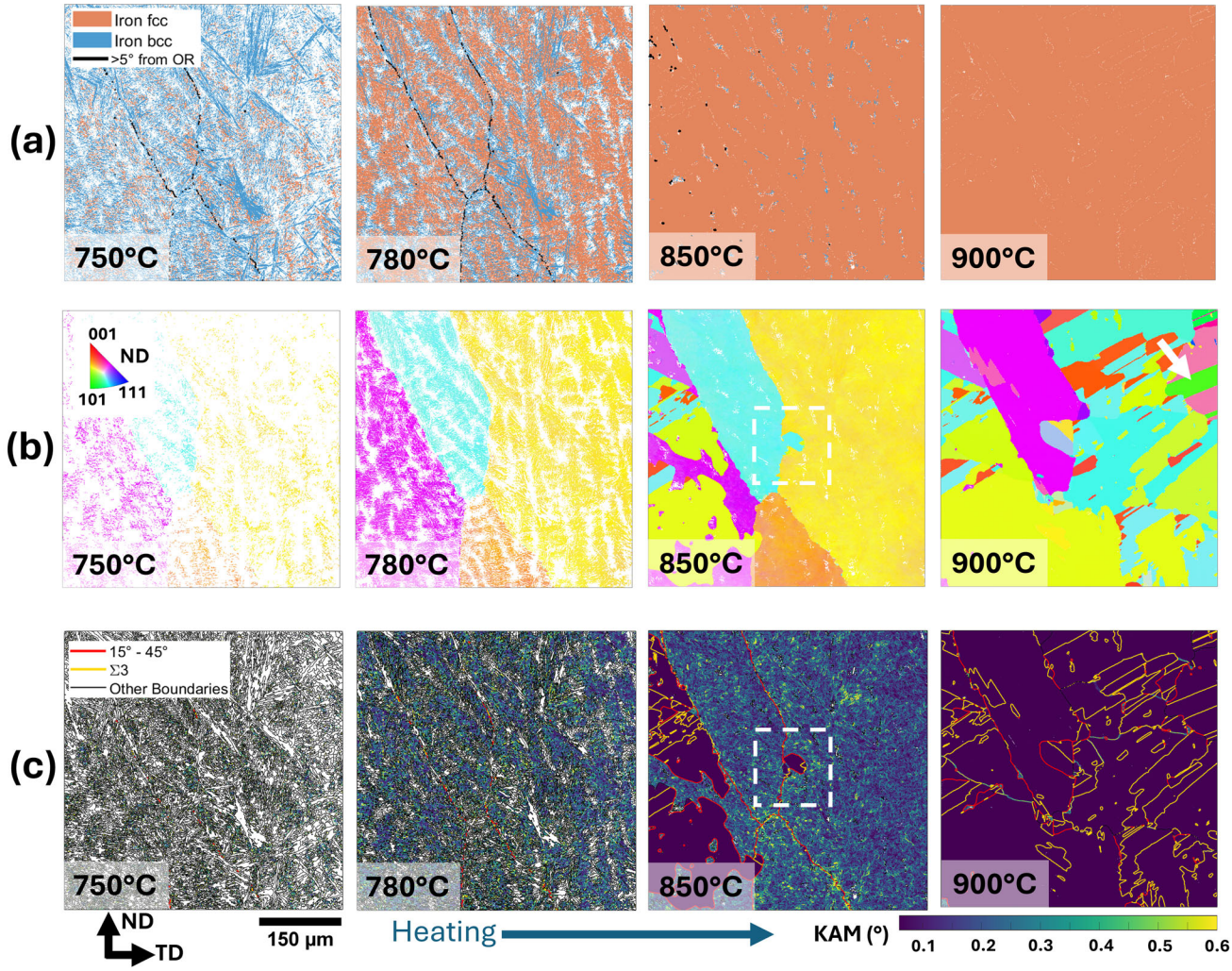


Fig. 10—Selected EBSD frames from the Test 1 (slow heating rate) *in-situ* EBSD experiment conducted with 300 M. The same four frames have been presented as: (*a*) phase maps with phase boundaries that do not obey an OR highlighted in black (> 5 deg), (*b*) EBSD orientation maps (FCC phase only) and (*c*) KAM maps with high-angle grain boundaries, twin boundaries and other boundaries highlighted in red, gold, and black, respectively. Dashed boxes indicate regions magnified in Figure 12. Animated GIFs using all frames can be found in Ref. [47] (Color figure online).

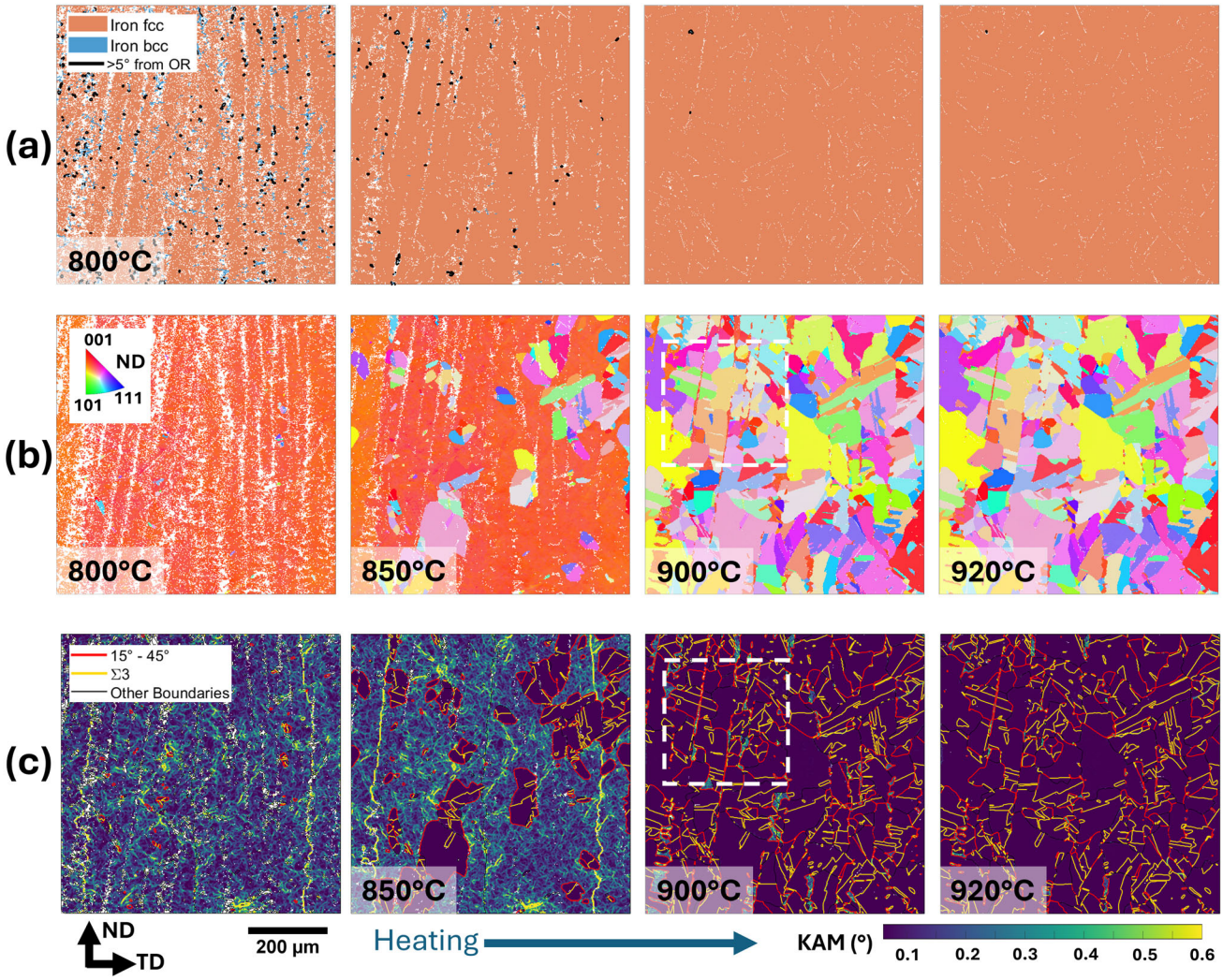


Fig. 11—Selected EBSD frames from the Test 2 (fast heating rate) *in-situ* EBSD experiment conducted with 300 M. The same four frames have been presented as: (*a*) phase maps with phase boundaries that do not obey an OR highlighted in black (> 5 deg), (*b*) EBSD orientation maps (FCC phase only) and (*c*) KAM maps with high-angle grain boundaries, twin boundaries and other boundaries highlighted in red, gold, and black, respectively. Dashed boxes indicate regions magnified in Figure 12. Animated GIFs using all frames can be found in Ref. [47] (Color figure online).

being developed during, and retained after, the phase transformation. This sub-structure formed by internal grain misorientations can be more easily viewed in the magnified KAM map in Figure 12(b).

For every EBSD frame still containing some original martensite and transformed austenite, the boundaries between the two phases could be compared with the OR calculated earlier using the pre-heating EBSD maps from Figure 8. In the Figures 10(a) and 11(a) phase maps, any phase boundaries that deviated more than 5 deg from this OR are highlighted in black, to indicate any martensite–austenite boundaries that did not follow an OR relationship. In Test 1, almost all the phase boundaries obeyed the OR, except those at the PAG boundaries [see black lines in Figure 10(a)]. The KAM maps in Figure 10(c) show the PAG boundaries are the only high angle grain boundaries present, and that strain induced boundary migration occurs *via* the bulging of PAG boundaries reformed through the memory effect as previously observed.[33] This behaviour is illustrated in the magnified areas in Figures 12(a) and (b). Careful analysis of the orientation maps [Figure 10(b)] reveals that all but one of the recrystallised grains (highlighted by a white arrow in the 900 °C frame) either retained an orientation present pre-recrystallisation, or were a twin of such orientations that existed pre-recrystallisation (*i.e.*, the only new orientations to form resulted from recrystallisation twinning). In some cases, grain boundary bulging may have initiated beneath the sample surface or outside the mapped region, as is likely for the grain highlighted by the white arrow in Figure 10(b).

Notably, in Test 2 several small non-OR boundaries can be seen distributed throughout the phase map and do not correspond to PAG boundaries [see the black lines in Figure 11(a)]. These boundaries correspond to a dispersion of small non-memory orientation grains that are just visible in the 800 °C frame [Figure 11(b)] and which eventually grow out to consume the memory orientation grains upon further heating, during what appears to be a different recrystallisation process with

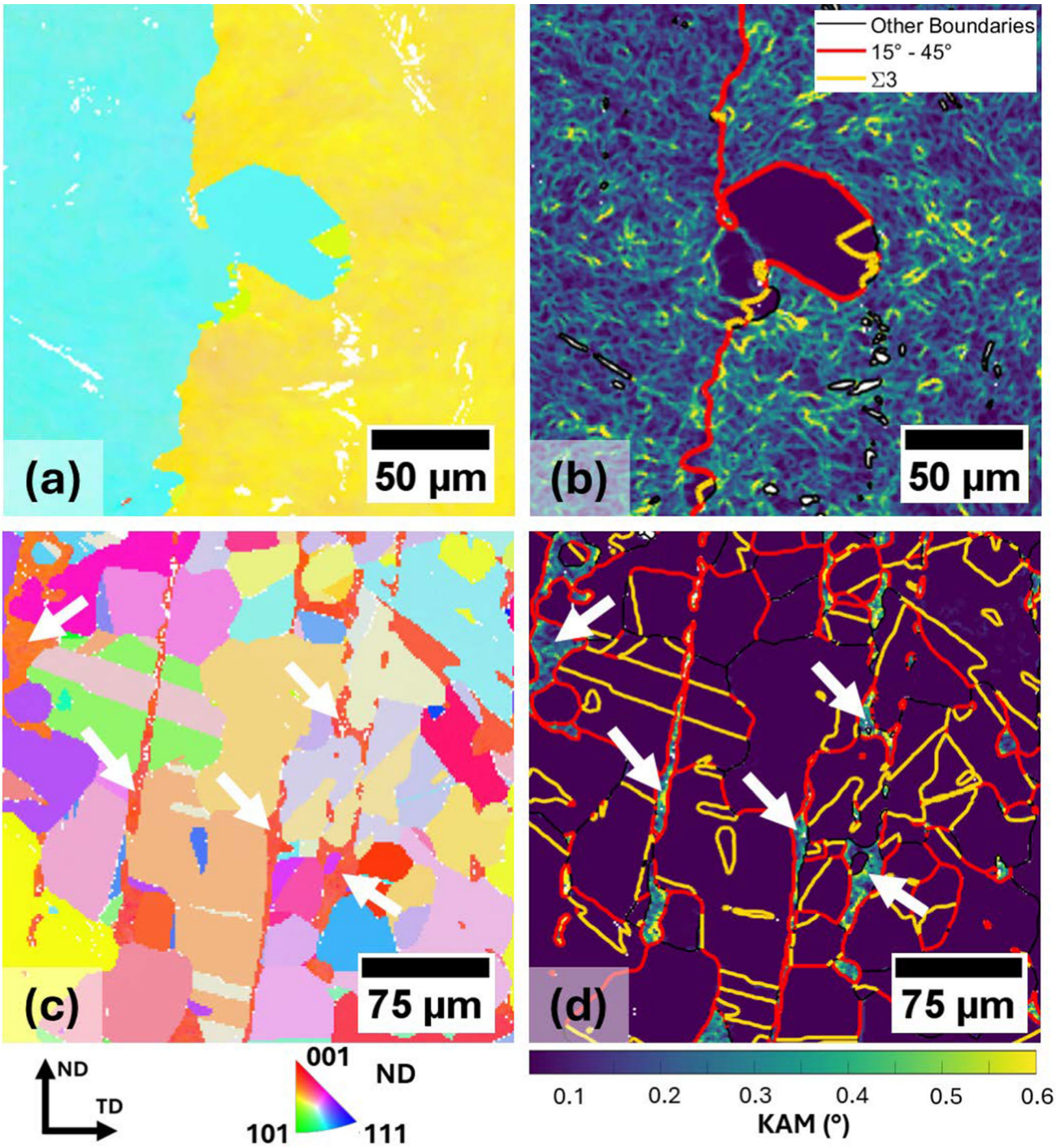


Fig. 12—(*a*) and (*b*) A magnified area from the Test 1 (300 M) 850 °C frame, also displayed in Figure 10. (*c*) and (*d*) A magnified area from the Test 2 (300 M) 900 °C frame, also displayed in Figure 11, memory orientation grains are highlighted by white arrows. Both areas are displayed as an FCC orientation map and a KAM map, respectively. In the KAM map high angle grain boundaries have been highlighted in red and twin boundaries in gold (Color figure online).

multiple nucleation points across reformed PAGs. KAM in (c) reveals that these grains contained very low internal misorientations and often shared high angle grain boundaries (15 deg to 45 deg) with the memory orientation grains, as is often found during strain induced boundary migration.[48] If the dataset is viewed as a GIF or 'video' (see link in Reference 47) these high angle boundaries can be seen to migrate faster than lower angle boundaries. Additionally, multiple twins were observed forming during the growth of these grains; however, no clear correlation was found between the timing or location of twin formation and the consumption of the memory orientation grains.

In both Test 1 and 2, the regions enriched by compositional microsegregation were observed to be the last regions to austenitise and contained the most mis-indexing [compare EDS in Figures 8(c) and (f) to EBSD Figures 10(a) and 11 (a)].

In both tests, the interdendritic areas acted as a barrier to the recrystallised grains, slowing their growth and causing them to grow around these regions (like a liquid moving around a solid obstacle). In some areas, it was the untransformed martensite during austenitisation, which was concentrated in the interdendritic regions, that provided these barriers, as has been reported previously.[33] Fine untransformed martensite may also have provided this barrier in many other interdendritic regions, but the indexing was poor in many of these areas and the step size in Test 2 may have been too coarse to detect it. Regardless, once the material had fully austenitised (*i.e.*, after the rest of the material had recrystallised around the interdendritic regions), this behaviour clearly led to incomplete recrystallisation by 920 °C, whereby regions of memory orientation austenite were retained with the morphology of the interdendritic regions, as highlighted by white arrows in Figures 12(c) and (d). In some cases, these regions actually austenitised with a memory orientation, after recrystallisation had completed in the rest of the material.

Finally, Figures 13(a) and (b) demonstrates that the recrystallised grains had low levels of internal lattice misorientations and could therefore be separated from the memory grains using the KAM averaged across each grain, commonly known as grain average misorientation (GAM), allowing the recrystallised area fraction to be calculated for each frame. This method was very effective for Test 2 as shown in (b), but was more challenging for the Test 1 dataset, shown in (a). This was because the recrystallisation mechanism in Test 1 occurred by grain boundary bulging, where the low internal misorientation recrystallised grains were still connected to the high internal misorientation grains that they bulged out from, with no grain boundary separating them because they remained part of the same grain. An example of this behaviour is highlighted by a white arrow in Figure 13(a). The GAM value for the whole of this grain was an average of the recrystallised and non-recrystallised halves, making them impossible to separate using a threshold. Nevertheless, the appearance of multiple twin boundaries, which separated out recrystallised grains did allow the recrystallised fraction for Test 1 to also be calculated. This is plotted against temperature for both tests in Figure 13(c). Interestingly, during Test 1, performed at a slower heating rate, the rate of recrystallisation begins to increase rapidly above 840 °C and almost, but not quite, reaches almost completion by the end of the experiment at 900 °C. In contrast, with a faster heating rate, recrystallisation appears to start at a much higher temperature in Test 2, but does not reach completion by the end of the experiment at 920 °C.

It must be remembered that the temperature values quoted for the *in-situ* EBSD work came from the thermocouple in the stage, not the sample surface, which can result in significant errors in the actual temperature. The *in-situ* EBSD results thus illustrates how the austenitisation and recrystallisation progress, but should not be used to measure the exact temperatures at which events occur.

E. *As-Built Microstructures of C465*

The as-built C465 microstructure contained martensite and retained austenite as can be seen from the EBSD band contrast, phase contrast and orientation maps in Figures 14(a) through (c). Predominantly, the crystallographic ⟨001⟩ poles of the retained austenite [Figure 14(c)] are commonly aligned with the normal direction, however, some other orientations are also present. Similar to 300 M the as-built WAAM C465 material also contained pronounced compositional microsegregation. The interdendritic regions in C465 were enriched in Ti, Ni and Mo [although only the Ti map is displayed in Figure 14(d)], and the majority of the retained austenite was found within these regions, as highlighted by the white arrow in Figure 14. Figure 14(e) displays a PAG reconstruction of the as-built EBSD map from Figures 14(a) through (c). Like the as-built 300 M microstructure, it contained large columnar PAGs with both the long dimension and the crystallographic ⟨001⟩ poles often aligned to the normal direction, and a minority fraction of other orientations were also present. The boundary map in Figure 14(f) then reveals that the majority of the grains that did not possess a ⟨001⟩ || ND alignment were in fact twins within columnar grains that did. Furthermore, plotting a pole figure of this map in Figure 14(g) shows that due to the strong ⟨001⟩ || ND fibre texture of the columnar grain, the ⟨111⟩ poles of the twin orientations were also commonly aligned with the normal direction.

F. *Austenitisation Behaviour of the C465 Dilatometry Samples*

A PAG reconstruction of a large area of the as-built C465 microstructure is displayed in Figure 15(a) to provide a direct comparison for the post-heat treatment PAG reconstructions. Figure 15(b) displays the EBSD PAG reconstructions of the C465 dilatometry samples heated to 982 °C at slow and fast heating rates, and then immediately quenched. Unlike for 300 M, the 0.1 °C s^{-1} sample was recrystallised, whilst the 100 °C s^{-1} sample displayed a memory effect only.

Figure 16(a) displays the EBSD PAG reconstructions of the C465 dilatometry samples that were heated, with various heating rates, to the conventional austenitisation temperature of 982 °C and held for 1 hour. All samples recrystallised irrespective of the heating rate, and heating rate had no obvious effect on PAG size between 0.1 °C s^{-1} and 100 °C s^{-1} (the area weighted equivalent circle diameter ranged from 103 μm to 92 μm in the 0.01 °C s^{-1} and 100 °C s^{-1} samples, respectively). EBSD PAG reconstructions of the samples heated to the intermediate temperature of 750 °C and held for 1 hour are shown in Figure 16(b), both the slow and fast heating rate samples displayed a memory effect only

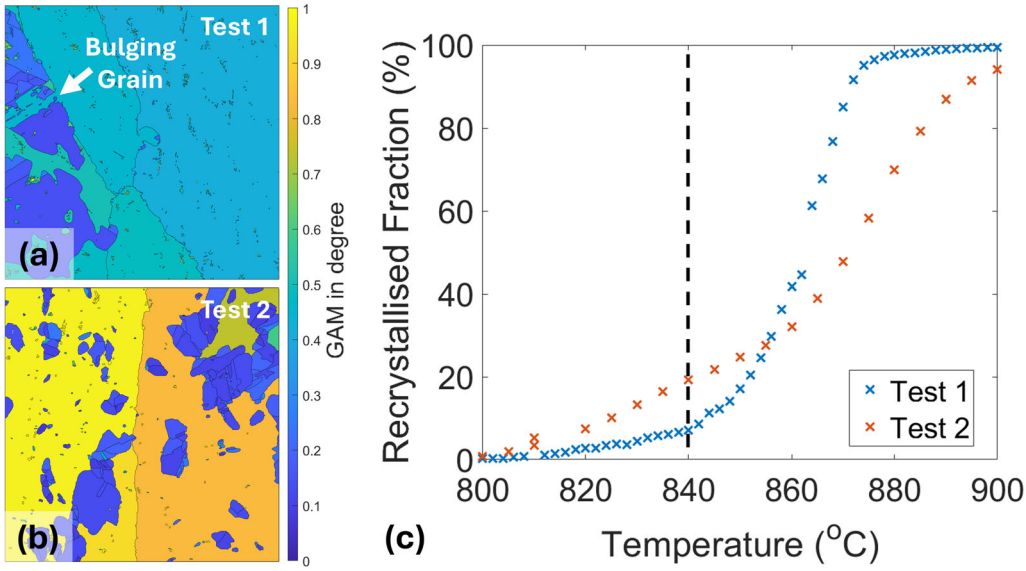


Fig. 13—(*a*) and (*b*) GAM maps from the 850 °C 300 M EBSD frames from Test 1 and 2 respectively (slow and fast heating rates). The same frames are also displayed in and. In (a) a white arrow has been added to indicate where a recrystallised grain has a high GAM since it is connected to the grain it bulged out from. (*c*) Recrystallised area fraction plotted against temperature for both tests, showing earlier onset in Test 2. A vertical dashed line has been added at 840 °C to highlight how the recrystallised fraction in Test 2 was higher at around this temperature range (Color figure online).

with no recrystallisation. Inverse pole figures (IPF) in Figure 16(c) illustrate how PAG reconstructions of the recrystallised samples still displayed a common fibre texture with the ⟨001⟩ poles aligned to the normal direction, although this was significantly weaker than the texture found in the as-built material. Only two IPF plots constructed from recrystallised samples are shown in Figure 16(c), but they are representative of all recrystallised C465 samples (the 10 °C s^{-1} sample had a noticeably stronger ⟨001⟩ || ND PAG texture than the other recrystallised samples, but this was still much weaker than in the as-built material). The second most common austenite texture component seen was the ⟨111⟩ poles aligned to the normal direction.

G. *Austenitisation Dilatometry Measurements of C465*

Figure 17(a) displays a dilatometry curve measured during the conventional 982 °C heat treatment performed on a C465 steel sample using a heating rate of 0.1 °C s^{-1}, the shape of this curve typified that measured during all C465 dilatometry tests. The temperature range over which C465 austenitises has been magnified in (b) and the other heating rates investigated with the conventional heat treatment have been plotted offset from the 0.1 °C s^{-1} curve. Like 300 M, increasing heating rate also increased the Ac_1 and Ac_3 temperatures in C465, although no additional contractions were observed during heating.

IV. DISCUSSION

A. *Austenitisation with a Memory Effect*

Historically, the austenite memory effect has probably been missed in many steels due to a lack of *in-situ* testing capabilities—if the steel is observed after a full recrystallisation step has finished, it would be impossible to recognise that a memory step had occurred. Here, in both steels, austenitisation proceeded *via* a memory effect (for all heating rates) and was followed by recrystallisation without the application of external deformation upon further heating (for some heating rates). This was observed directly *in-situ* for 300 M, but can be inferred for C465 based on the observation that textured columnar grains were found in the PAG reconstructions of the samples heated to and held at the lower temperature of 750 °C in Figure 16(b) (above Ac_3 measured by dilatometry), but not those heated further to 982 °C in Figure 16(a) [apart from when the fastest heating rate was used with no hold at peak temperature in Figure 15(b)]. The fact that memory and recrystallisation were found in these two very compositionally different martensitic steels, and have also been reported in the literature[10–18] for other alloys, implies that these effects may be common during the austenitisation of martensitic steels more generally.

B. *Conditions for Recrystallisation in 300 M and C465*

The observation that both 300 M and C465 samples heated at 100 °C s^{-1} and quenched without a hold [see Figures 3(d) and 15 (b)] exhibited a memory effect without recrystallisation highlights two key points: (1) even at the fastest heating rates, the memory effect

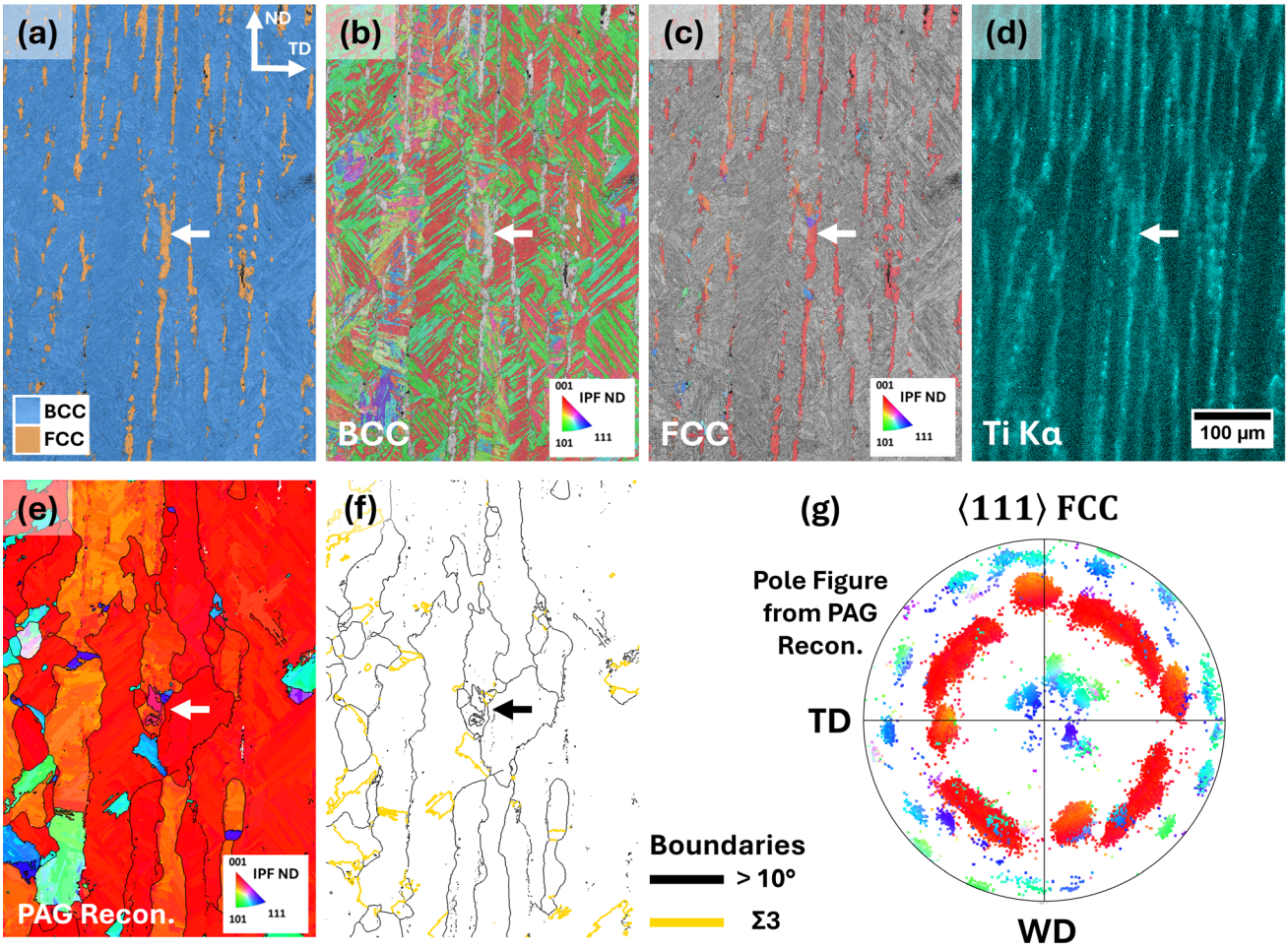


Fig. 14—A small-area EBSD map with simultaneous EDS of C465 in the as-built condition. (*a*) through (*c*) The phase colour map, the inverse pole figure (IPF) maps for the BCC phase and the IPF map for the FCC phase, respectively. All are overlaid with band contrast and the IPF orientations are aligned to the build normal direction. (*d*) The corresponding EDS map showing Ti Ka intensity. An arrow is positioned at the same location on each map. (*e*) A PAG reconstruction of the same EBSD map, also displayed in (a) through (c), here presented as an orientation map. (*f*) The same PAG reconstruction showing only grain boundaries, Σ3 boundaries are highlighted in gold. (*g*) A pole figure from the same reconstruction showing all pixels, coloured as they were in (e) (Color figure online).

precedes recrystallisation, and (2) recrystallisation requires a minimum time at temperature to occur, and can be suppressed entirely if the heat treatment is too brief. In 300 M, recrystallisation may also be supressed if there is sufficient time for recovery before the onset of recrystallisation, as seen in the 0.01 °C s^{-1} heating rate sample [Figure 4(a)]. However, recrystallisation was not supressed in the equivalent C465 sample [0.01 °C s^{-1} to 982 °C in Figure 16(a)]. This may have been related to the lower austenitisation temperatures in C465 compared with 300 M (Ac_1 = 497 °C at 0.01 °C s^{-1} in C465 *vs* 739 °C in 300 M) and potentially the lower recrystallisation temperature too. Both of these will have led to less opportunity for recovery, despite the larger temperature gap between the start of austenitisation and of recrystallisation in C465. *In-situ* EBSD experiments and the 840 °C peak temperature dilatometry tests demonstrate that in 300 M, recrystallisation started before austenitisation was completed, whilst the C465 dilatometry samples heated to 750 °C displayed no evidence of recrystallisation regardless of heating rate [Figure 16(b)]. Although the recrystallisation temperature of C465 for a given heating rate was not measured in this study, it must have been above 750 °C and the Ac_3 temperature of C465 as measured at heating rates up to 1 °C s^{-1} (739 °C). Independent annealing studies on cold-rolled plates[49] have shown a significant reduction in grain size when C465 is heated above 800 °C. Moreover, the slow heating rate (0.1 °C s^{-1}) C465 sample immediately quenched after reaching peak temperature [Figure 15(b)] likely recrystallised where its fast heating rate (100 °C s^{-1}) counterpart did not, because it exceeded the temperature required for recrystallisation for an ample time to allow recrystallisation during further heating to 982 °C. Further details regarding the recrystallisation behaviours of 300 M and C465 are discussed in the following sections.

1. *Recrystallisation behaviour in 300 M*

Recrystallisation in 300 M was evidently sensitive to heating rate and hold time. The dilatometry PAG reconstructions in Figure 4(a) illustrated that increasing

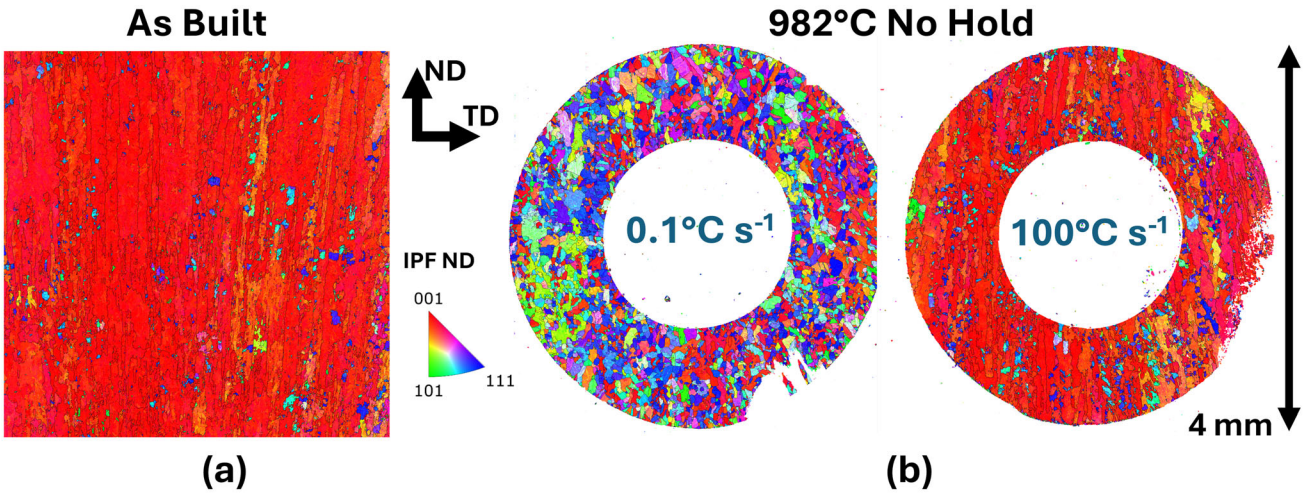


Fig. 15—(*a*) A large-area EBSD PAG reconstruction of the as-built C465 microstructure. (*b*) EBSD PAG reconstructions of the C465 dilatometry sample cross-sections heated to 982 °C and immediately quenched, at slow and fast heating rates, respectively.

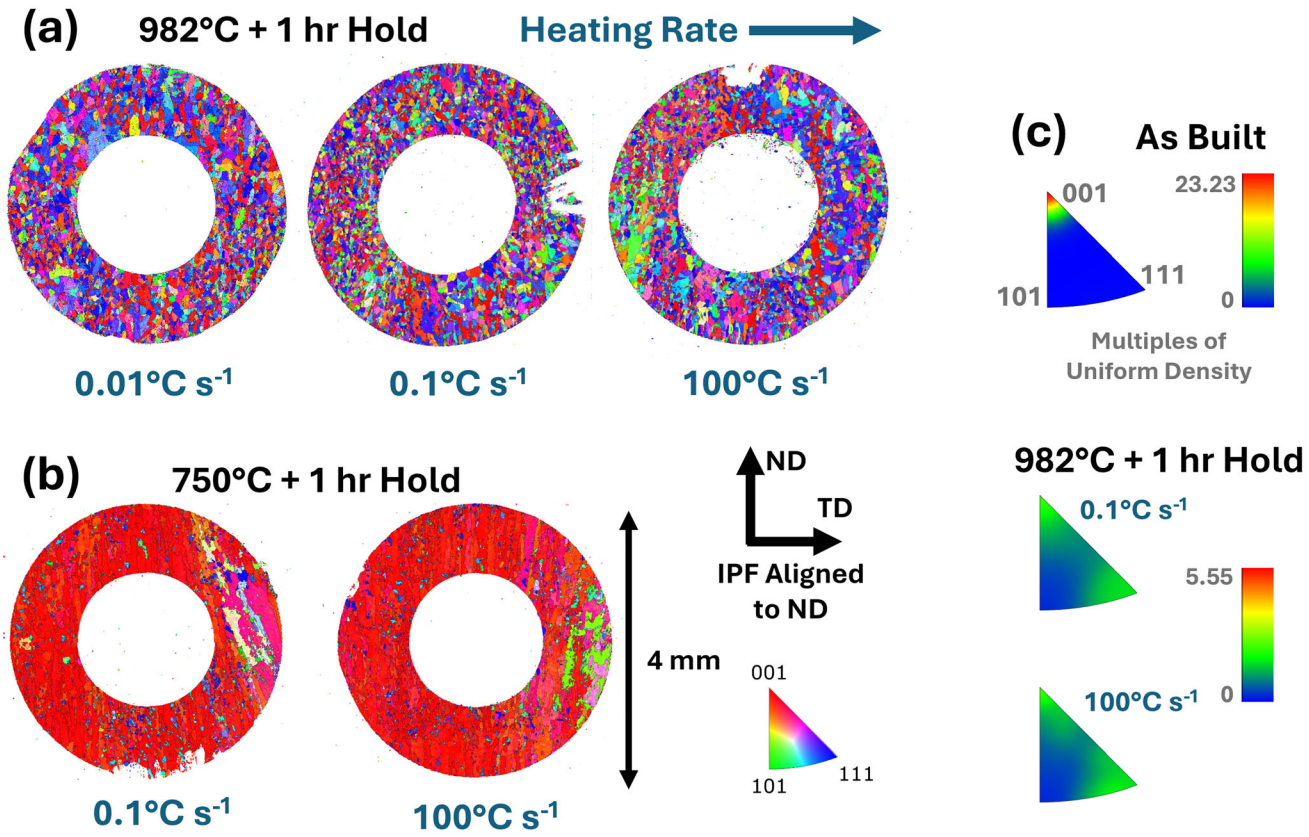


Fig. 16—EBSD PAG reconstructions from the C465 dilatometry investigation. (*a*) The 982 °C and 1 h hold samples with varying heating rates. (*b*) The samples heated to the lower 750 °C austenitisation temperature and held for 1 h with slow and fast heating rates. (*c*) IPF plots constructed from PAG reconstructions showing FCC texture evolution in the as-built material [Figure 15(a)] and in slow and fast heating rate 982 °C and 1 h hold dilatometry samples after recrystallisation.

heating rate invoked a transition from a memory effect only (0.01 °C s^{-1}), to recrystallisation (0.1 °C s^{-1} onwards), and then to recrystallisation with greater PAG refinement (0.5 °C s^{-1} onwards). Although the temperature profiles of the *in-situ* experiments do not correspond to those used for the dilatometry experiments, the *in-situ* tests do represent scenarios where a sample has had more or less time available for recovery in Test 1 and Test 2, respectively. Thus, they can be used to gain a mechanistic understanding of the change in

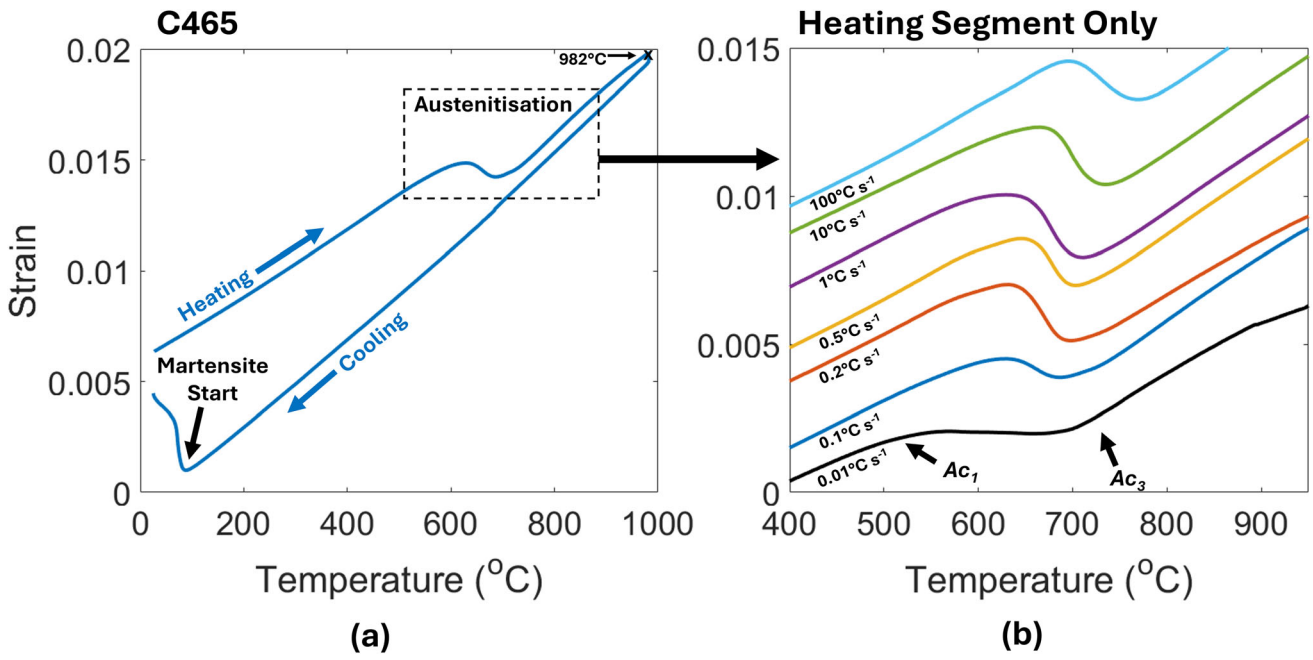


Fig. 17—(*a*) The full dilatometry curve for the C465 0.1 °C s^{-1} heating rate to 982 °C test, with a 1 h hold at temperature, key features in the curve are highlighted. (*b*) The heating data between 500 °C and 910 °C from the boxed section in (a). The same region from the other the C465 dilatometry curves with different heating rates are also displayed, their strain has been offset to allow for direct comparison.

recrystallisation behaviour with heating rate. Decreasing the time available for recovery (or increasing heating rate) shifts the mechanism from strain induced boundary migration through the bulging of the reformed high angle PAG boundaries (exemplified by Test 1 in Figure 10), to one in which new, comparatively strain free, austenite grains appear to nucleate within the reformed PAGs (exemplified by Test 2 in Figure 11). The larger PAG size in the 0.1 °C s^{-1} and 0.2 °C s^{-1} heating rate dilatometry samples (244 μm and 175 μm, respectively) would suggest that the grain boundary bulging mechanism was responsible for recrystallisation, and that this transitioned to the mechanism involving the nucleation of new grains above 0.5 °C s^{-1} (110 μm). It is possible that the slow heating rate samples also recrystallised *via* the nucleation of new austenite grains, but with fewer nuclei resulted in a larger final grain size. However, it is very unlikely that post-recrystallisation grain growth was responsible for their larger grain size. Minimal austenite grain growth was observed after recrystallised grains had impinged during either *in-situ* experiment, both of which had far slower heating rates than the 0.1 °C s^{-1} dilatometry tests during the EBSD sections of their temperature profiles (0.02 °C s^{-1} in Test 2). Furthermore, significant austenite grain growth was not expected in 300 M at these temperatures based on literature.[1,2,50–53]

Importantly, both recrystallisation mechanisms were observed to lead to austenite grain refinement. During the bulging of high angle boundaries (Test 1), this refinement was due to the formation of recrystallisation twins during boundary migration—without these twins the austenite grain morphology may change, but no new crystallographic orientations would have been introduced and refinement would have been limited or nil. The mechanism of refinement seen here is akin to that described for the recrystallisation of martensite by Tsuchiyama *et al.*,[48] although here refinement is reduced by the scale and morphology of the columnar PAGs, which share high angle boundaries with fewer neighbours per unit length of boundary. It is thus hypothesised that, if the material were to be re-austenitised and quenched a second time (*i.e.*, a cyclic heat treatment), further grain refinement would occur as further twinning would likely take place, and the austenite grain morphology would be broken up by boundary bulging.

In comparison, the nucleation of new austenite grains (Test 2) was a far more effective recrystallisation mechanism for grain refinement. This mechanism was similar to that reported by Ressel *et al.*,[17] who found that increasing heating rate increases the density of new grains formed, and thus decreases the final austenite grain size achieved. The dilatometry experiments here suggest that something similar may have occurred, as PAG size decreased with increasing heating rate between 0.5 °C s^{-1} (110 μm area weighted equivalent circle diameter) and 10 °C s^{-1} (77 μm). However, it was unclear whether this was significant as the PAG size increased again for the 100 °C s^{-1} heating rate (111 μm). The final PAG size may have been influenced by the size of the initial columnar PAGs, which will have varied from sample to sample depending on where they came from in the WAAM build. Alternatively, carbide dissolution and boundary pinning effects will have varied with heating rate as demonstrated by Figure 6.

It is possible that the new recrystallised grains may originate from non-memory-effect orientations that form during austenitisation,[21] which then grow out, rather than the sub-grains formed in the dislocation dense memory orientation austenite.[15] Unfortunately, the EBSD maps collected during the Test 2 *in-situ* experiment did not have the spatial or temporal resolution to reveal the origins of the new austenite grains with any confidence, although some of the recrystallised grain orientations were present during austenitisation in the first EBSD frame collected [Figure 11(b)]. During austenitisation *via* a partial memory effect, the austenite grains that share no OR with surrounding martensite have often been found to nucleate at PAG boundaries.[10,11,13–15,17–19,22,23,26] Strangely, in Test 2, these grains appear in the centre of PAGs, as seen when comparing the Figure 11(a) phase map with no OR boundaries in black with the PAG reconstruction in Figure 8(e). It is possible that these grains nucleated/grew from memory grain boundaries beneath the surface. However, this seems unlikely to account for all these grains, given their numbers and range of crystallographic orientations in comparison to the columnar memory grains. It should be noted that the two recrystallisation mechanisms observed here are not necessarily mutually exclusive, and may occur simultaneously. This may have been true for the 0.2 °C s^{-1} heating rate dilatometry sample which had a grain size between that of the 0.1 °C s^{-1} and 0.5 °C s^{-1} samples (175 μm compared with 244 μm and 110 μm, respectively).

Finally, the results of the two dilatometer heat treatments to the lower 840 °C hold temperature in Figure 4(b) present an interesting scenario. In this case, the 100 °C s^{-1} heating rate sample recrystallised, similar to its 871 °C s^{-1} peak temperature counterpart, presumably through the nucleation of new austenite grains. In contrast, there was only limited evidence of recrystallisation in the 0.1 °C s^{-1} sample, whereas it's 871 °C peak temperature counterpart did recrystallise, most likely *via* a grain boundary bulging mechanism. The reason why the 840 °C/0.1 °C s^{-1} sample did not recrystallise and the 871 °C/0.1 °C s^{-1} did may be explained using the *in-situ* EBSD recrystallised fractions plot in Figure 13(c). During Test 2, recrystallisation started at a lower temperature following austenitisation than during Test 1, even though upon further heating recrystallisation progressed to completion at a faster rate during Test 1. The black dashed line on Figure 13(c) shows how the 840 °C dilatometry samples may have been held in the temperature region where recrystallisation *via* the nucleation of new grains had started for the faster heating rate, but recrystallisation *via* high angle grain boundaries had not begun in earnest. Of course, this is based on the reasonable assumption that that the temperature gradient between the sample surface and the location of the thermocouple underneath was similar during both *in-situ* experiments, such that the recrystallised fraction at a given temperature could be compared. The temperatures at which events occurred during the *in-situ* experiments should not be taken as the exact temperatures at which they would occur *ex-situ* due to this temperature gradient (thought to be < 20 °C based on previous work).

Reduced time for recovery during Test 2 may have resulted in a greater driving force for recrystallisation, enabling it to take place at lower temperatures than in Test 1. The change in recrystallisation mechanism may also have played a role in altering the recrystallisation start temperature, potentially the high angle grain boundary bulging mechanism could be hindered by pinning by carbides already present at PAG boundaries, whereas the new austenite grains nucleated within PAGs were not. However, no evidence was found to support this and the growth of recrystallised grains in Test 2 did not appear to be hindered by PAG boundaries. Regardless of the mechanism, the 840 °C peak temperature tests provide another example where heating rate may alter the temperatures at which recrystallisation occurs.

Overall, the time available for recovery above Ac_1, and therefore heating rate, has been shown to greatly alter the level of grain refinement achieved in 300 M during an austenitisation heat treatment. For industrial applications, a cyclic austenitisation treatment may therefore be used to produce a fine-grained microstructure from an additively manufactured part, provided the heating rate above Ac_1 is sufficient. In contrast, if it is not, or the austenitisation temperature is too low, or the hold time at temperature is too short, this will be detrimental to grain refinement.

2. *Non-linear heating rates in 300 M*

The 0.01 → 100 °C s^{-1} heating profile dilatometry experiments using 300 M were intended to investigate whether the heating rate before austenitisation affected recrystallisation, or whether only the heating rate through and after austenitisation were of significance. This alluded to the question: is the austenite dislocation density, which must be driving recrystallisation, generated during the phase transformation[23,24] or inherited from the prior-martensite?[12,15,29] If it was generated during the phase transformation, the 0.01 → 100 °C s^{-1} sample held at 871 °C for 1 hour should recrystallise like its 100 °C s^{-1} heating rate counterpart. If it was inherited, then the martensite should have had sufficient time to recover during the slow section of the heating profile, and the sample should have displayed only a memory effect like its 0.01 °C s^{-1} counterpart.

Unexpectedly, both 0.01 → 100 °C s^{-1} heating profile samples (Figure 5) displayed evidence of a memory effect and partial recrystallisation. The fact that recrystallisation occurred at all would suggest that dislocations were predominantly generated during the phase transformation. Additionally, recrystallisation is likely to have been similar to that found in the samples heated with a constant heating rate of 100 °C s^{-1}, in that many austenite grains with new orientations evidently nucleated throughout the large columnar memory orientation PAGs. However, growth and eventual impingement of these new grains did not progress to completion. This is likely due to the recrystallised grains being pinned by carbides that grew during the slow 0.01 °C s^{-1} heating segment—see the dilatometry carbide peak in Figure 7(b) and the carbides imaged in the

0.01 → 100 °C s^{-1} sample immediately quenched from 871 °C shown in Figure 6(a). The same coarse carbides did not have sufficient time to form in samples heated with a constant rate of 100 °C s^{-1} as evidenced by their absence Figure 6(b). In the slower constant heating rate samples, the carbides formed (as evidenced in the curves dilatometry) but had sufficient time to dissolve during slower heating to, or holding at, 871 °C.[1,4,50] This was illustrated by the lack of very coarse carbides present in the 0.1 °C s^{-1} sample in Figure 6(c) in comparison with Figure 6(a).

It was unclear why the two stage 0.01 → 100 °C s^{-1} sample that was immediately quenched after reaching peak temperature displayed evidence of recrystallisation, whilst the other 300 M samples heated at a constant rate and quenched immediately did not. It is worth noting that recrystallisation in the 0.01 → 100 °C s^{-1} immediately quenched sample did appear to be in its early stages, since the non-memory orientation grains were larger in equivalent sample that was held for 1 hour [compare Figures 5(a) and (b)]. It is possible that the increased density of coarse carbides may have affected austenitisation behaviour *via* the memory effect (Ac_1 was approximately 20 °C higher in the two stage heat treatment samples compared with those heated at a constant 100 °C s^{-1} only), or that the presence of the carbides influenced the nucleation of recrystallised non-memory orientation grains in some other way and could warrant its own investigation.[20] Although, this case is unlikely to be industrially relevant since the heat treatment used was extreme (the heating rate used through austenitisation was very fast), it does highlight how undissolved carbide populations may significantly hinder recrystallisation. Further study including the high temperature measurement of dislocation density during austenitisation needed to fully investigate the origin of austenite dislocation density during the memory effect.

3. *Recrystallisation behaviour in C465*

PAG refinement in C465 was far less sensitive to heating rate than 300 M, as can be seen from the relatively consistent PAG size across all heating rates in C465 after holding at 982 °C for 1 hour [Figure 16(a)]. This suggests that recovery over the temperature range between Ac_1 and the start of recrystallisation was insufficient to produce a difference in recrystallisation behaviour over the range of heating rates investigated. It may also be inferred that the mechanism for recrystallisation in this alloy may have been consistent over the range of heating rates investigated, and may have been similar to that observed in PH 13-8 Mo by Rosenauer *et al.*[18] It is likely that in C465 recrystallisation occurred primarily through the strain induced migration of pre-existing high angle grain boundaries, similar to the mechanism observed in 300 M at the 0.1 to 0.2 °C s^{-1} heating rates and in the Test 1 *in-situ* experiment. This can be inferred from the fact that recrystallised C465 developed a texture with the ⟨001⟩ poles or ⟨111⟩ poles commonly aligned with the normal [(or build) direction as seen in Figure 16(c)] and the pole figure in Figure 14(g) demonstrated that the same textures were present in the PAG reconstruction of the as-built material, although the ⟨111⟩ texture was less prevalent pre-recrystallisation. This would strongly suggest that new austenite grains were not nucleated during recrystallisation in C465, as if they had, a more random texture would be expected as found in the fast-heating rate 300 M dilatometry samples, or the Test 2 *in-situ* experiment. The same austenite orientations exist before and after recrystallisation, but through grain boundary migration the area fraction of ⟨111⟩ || ND textured grains increased after recrystallisation, reducing the overall ⟨001⟩ || ND. It still remains unclear why the strong texture components were not further broken up by recrystallisation twinning (as-opposed to twins reformed during the memory effect) as was observed *in-situ* during strain induced boundary migration in austenitised 300 M (Test 1 in Figure 10). Future work could address this by conducting high-temperature *in-situ* EBSD or interrupted heat treatments with intermediate EBSD mapping. These approaches would also help confirm whether the observed texture evolution results from strain induced boundary migration, twinning, or other mechanisms.

Figures 14(e) and (f) illustrated that the small ⟨111⟩ || ND texture PAGs in the as-built material originated from twinning in the strongly ⟨001⟩ || ND textured columnar grains. Recrystallisation by strain induced boundary bulging may produce more effective PAG refinement in C465 than in 300 M due to the finer PAG structure of the as-built material and due to the dispersion of twins throughout the material. Although the small grains may not migrate into the grains with which they share a twin relation, they may into the neighbouring grains with which they are not twinned, and with which they share a HAGB. Thus, by growing larger and competing with the ⟨001⟩ || ND textured grains they increase PAG refinement in the material overall and break up the columnar morphology.

Taken together, these observations suggest that the final grain size in C465 may be governed by the distribution of twin-related orientations in the retained or memory orientation austenite, rather than by the nucleation of new austenite grains. This would explain why heating rate had little effect on the final grain size. However, the possibility that recrystallisation occurs by the nucleation of new grains cannot be completely ruled out. It is also unclear why the as-built C465 PAG structure contains a significant distribution of twins, when 300 M does not ('islands' of small grains found within columnar PAGs in Figure 3(c) are likely mis-reconstructed larger twins[54–57]). It is possible that this is related to the different conditions experienced during WAAM.

C. *The Effect of Compositional Microsegregation*

In both 300 M *in-situ* EBSD experiments, compositionally enriched (interdendritic) areas of microsegregation were present in the WAAM starting material [Figures 8(c) and (f)]. These austenitised at higher temperatures than depleted regions [see Figures 10(a) and 11(a)]. This was the opposite trend from what might

be expected under equilibrium conditions, given that these regions were enriched in Ni, Cr, Mo and Si, elements that are expected to lower the austenite start temperature. SE images recorded during austenitisation (Figure 9) show particles coarsening, concentrated in the same interdendritic regions first. It is reasonable to assume that these particles are carbides based on prior knowledge of 300 M,[1,4,45,50] *ex-situ* imaging of similar carbides in Figure 6 and the volume change associated with carbide formation seen in the dilatometry curves in Figures 7(a) and (b). It is thus postulated that the localisation of alloy carbides to the enriched regions depleted these regions of carbon; since carbon has a much great effect on Ac_1 than any other alloying element in 300 M,[58–60] this may have raised the Ac_1 temperature locally and hence meant that the interdendritic regions austenitised last. That is not to say that carbides were not stable in the rest of the material, only that a higher volume fraction of carbides were stable in the regions enriched in alloying elements, across a wider temperature range as has been observed previously in similar steels.[61] This idea is supported by the fact that in Figure 6(c), the carbides which survived heating to 871 °C at 0.1 °C s^{-1}, were concentrated in the compositionally enriched regions.

Interestingly, in Test 2, the recrystallised grains appear to be impinged on the later austenitising compositionally enriched regions, allowing an interdendritic pattern of memory orientation grains with high internal misorientation to survive to 920 °C as shown in Figures 12(c) and (d). This may be in part due to the boundary pinning effect of carbides concentrated in these regions, or the higher concentration of slow diffusing elements segregated in solid solution. However, in some cases the recrystallised grains were pinned by the later-transforming martensite also found in these regions. Regardless, when the recrystallised grains grow into the interdendritic memory effect grains upon further heating, the elongated the shape of these regions cause the recrystallised grains to form long straight austenite boundaries across the microstructure. If only viewing a post-heat treatment PAG reconstruction, it would be easy to assume that these lines trace out the original columnar grain structure. However, they align with the interdendritic regions formed during initial solidification from the weld melt pool, not the columnar grain formed during the reheating from subsequent weld passes.

The effect of compositional microsegregation on austenite recrystallisation behaviour in C465 was less clear. It is plausible that recrystallised austenite grains could be impinged on interdendritic regions as was observed *in-situ* for 300 M (Test 2), thus microsegregation could influence final grain size. However, it is impossible to say without *in-situ* work or comparing sample with differing dendrite spacing. Further work is warranted to investigate how WAAM-induced segregation affects not only recrystallisation behaviour, but also the mechanical and corrosion properties of these alloys.

D. *Implications for Heat Treatment Design for Refinement of Coarse PAGs*

The distinctive as-built microstructures produced by WAAM provided a challenging but informative platform for studying PAG refinement during austenitisation. Whilst the findings are directly applicable to WAAM components, they also offer broader insights for heat treatment design in steels with coarse PAGs but manufactured using other technologies. In both 300 M and C465, the memory effect can severely limit grain refinement if the austenitisation temperature or hold time is insufficient. However, C465 showed robust recrystallisation behaviour across a range of conditions, whereas 300 M required rapid heating above Ac_1 to achieve effective refinement. These results highlight the need for alloy-specific thermal strategies: for 300 M, heating rates above 0.5 °C s^{-1} are recommended to suppress recovery and promote recrystallisation, whilst C465 offers more flexibility. These insights can inform the development of tailored heat treatments for a range of high-performance steels, particularly in additive manufacturing contexts where coarse PAGs are prevalent.

V. CONCLUSIONS

This study investigated the influence of heating rate and hold time on austenitisation and grain refinement from 300 M and C465 steels with coarse PAG structures. The following conclusions were drawn:

- Both 300 M and C465 exhibited a memory effect during austenitisation regardless of heating rate. This was sometimes, but not always, followed by autogenous recrystallisation upon further heating (without the application of external deformation).
- In 300 M, recrystallisation behaviour was highly sensitive to heating rate and recovery time. Slow heating allowed recovery to suppress recrystallisation, whilst faster heating promoted either strain induced boundary migration or nucleation of new grains, depending on the rate. A hold at the austenitisation temperature was essential for recrystallisation to complete, although it could be affected by boundary pinning carbides coarsened by slow heating rates below Ac_1.
- Slower heating rates were found to raise the temperature at which recrystallisation started in 300 M. This was believed to be because there was time for some recovery post-austenitisation during slow heating rates, reducing the driving force for recrystallisation.
- In contrast to 300 M, C465 showed less sensitivity to heating rate. Recrystallisation occurred more consistently and appeared to proceed primarily *via* strain induced boundary migration, retaining the crystallographic texture of the as-built material. Grain refinement was more closely linked to the distribution of twins in the initial microstructure.
- Compositional microsegregation in 300 M locally delayed austenitisation and influenced

recrystallisation morphology, leading to elongated retained memory regions shaped by interdendritic segregation.
- For both alloys, a post-build austenitisation treatment can refine prior austenite grains. However, 300 M requires careful control of heating rate and hold time to avoid incomplete recrystallisation, whilst C465 is more robust but still benefits from sufficient holding time.

These findings offer clear guidance for designing austenitisation heat treatments in steels with coarse PAGs, particularly those produced by additive manufacturing. Crucially, they demonstrate that a one-size-fits-all approach is insufficient: 300 M requires precise thermal control to unlock grain refinement, whilst C465 is more forgiving but still demands adequate thermal exposure. Understanding and leveraging these alloy-specific behaviours is essential for advancing the performance and reliability of next-generation structural components.

ACKNOWLEDGMENTS

This work was undertaken within the ATI I-Break project led by Airbus. I-Break is a collaborative research project involving multiple UK partners to develop alternatives to forging manufacturing technology for landing gear applications. The authors gratefully acknowledge financial support from Innovate UK (project reference 10003486). The authors acknowledge the use of equipment associated with the Advanced Metals Processing and Characterisation themes of the Henry Royce Institute for Advanced Materials, funded through EPSRC grants EP/R00661X/1, EP/S019367/1, EP/P025021/1 and EP/P025498/1. Animated GIFs can be found by following the link in Reference 47 and the raw data associated with this manuscript can be found by following the link in Reference 40.

CONFLICT OF INTEREST

The authors declare that they have no known competing financial interests or personal relationships that could have appeared to influence the work reported in this paper.

OPEN ACCESS

This article is licensed under a Creative Commons Attribution 4.0 International License, which permits use, sharing, adaptation, distribution and reproduction in any medium or format, as long as you give appropriate credit to the original author(s) and the source, provide a link to the Creative Commons licence, and indicate if changes were made. The images or other third party material in this article are included in the article's Creative Commons licence, unless indicated otherwise in a credit line to the material. If material is not included in the article's Creative Commons licence and your intended use is not permitted by statutory regulation or exceeds the permitted use, you will need to obtain permission directly from the copyright holder. To view a copy of this licence, visit http://creativecommons.org/licenses/by/4.0/.

SUPPLEMENTARY INFORMATION

The online version contains supplementary material available at https://doi.org/10.1007/s11661-026-08241-9.

REFERENCES

1. L. Youngblood and Raghavan, M, microstructure and mechanical properties of quenched and tempered 300M steel. (1978). No. NASA-TP-1288.
2. W.-D. Cao and X.-P. Lu: *Metall. Trans. A*, 1987, vol. 18, pp. 1569–85.
3. Y. Tomita: *Mater. Sci. Technol.*, 1991, vol. 7, pp. 97–104.
4. Y. Xiong, D. Wen, Z. Zheng, C. Sun, J. Xie, and J. Li: *Mater. Charact.*, 2023, vol. 198, p. 112756.
5. J. Wang, M. Taylor, C. Diao, E. Pickering, J. Qin, Y. Lu, S.M. Meco, J. Ding, and S. Williams: *Add. Manuf. Lett.*, 2025, vol. 14, p. 100307.
6. J. Wang, C. Diao, M. Taylor, C. Wang, E. Pickering, J. Ding, M. Pimentel, and S. Williams: *Int. J. Adv. Manuf. Technol.*, 2023, vol. 129, pp. 3751–67.
7. T.A. Rodrigues, V.R. Duarte, D. Tomás, J.A. Avila, J.D. Escobar, E. Rossinyol, N. Schell, T.G. Santos, and J.P. Oliveira: *Add. Manuf.*, 2020, vol. 34, p. 101200.
8. Y. Xu, B. Mishra, and S.P. Narra: *Mater. Charact.*, 2022, vol. 190, p. 112065.
9. J. L'Hostis, L. Thuinet, E. Cadel, and M.-N. Avettand-Fènoël: *Acta Mater.*, 2025, vol. 291, p. 120972.
10. S. Matsuda and Y. Okamura: *ISIJ Int.*, 1974, vol. 14, pp. 444–49.
11. S.T. Kimmins and D.J. Gooch: *Metal Sci.*, 1983, vol. 17, pp. 519–32.
12. S.S. D'yachenko: *Metal Sci. Heat Treat.*, 2000, vol. 42, pp. 122–27.
13. T. Shinozaki, Y. Tomota, T. Fukino, and T. Suzuki: *ISIJ Int.*, 2017, vol. 57, pp. 533–39.
14. Y. Tomota, W. Gong, S. Harjo, and T. Shinozaki: *Scripta Mater.*, 2017, vol. 133, pp. 79–82.
15. H. Shirazi, G. Miyamoto, S.H. Nedjad, T. Chiba, M.N. Ahmadabadi, and T. Furuhara: *Acta Mater.*, 2018, vol. 144, pp. 269–80.
16. D. Brandl, M. Lukas, M. Stockinger, S. Ploberger, and G. Ressel: *Mater. Des.*, 2019, vol. 176, p. 107841.
17. G. Ressel, D. Brandl, T. Hönigmann, M. Lukas, A. Stark, C. Gruber, S. Lukas, M. Stockinger, and E. Kozeschnik: *Mater. Des.*, 2023, vol. 234, p. 112370.
18. A. Rosenauer, D. Brandl, G. Ressel, T. Hönigmann, M. Stadler, C. Turk, C. Gammer, M. Wiessner, E. Gamsjäger, M. Stockinger, and R. Schnitzer: *Mater. Charact.*, 2024, vol. 208, p. 113554.
19. S. Matsuda and Y. Okamura: *ISIJ Int.*, 1974, vol. 14, pp. 363–68.
20. S. Watanabe and T. Kunitake: *ISIJ Int.*, 1976, vol. 16, pp. 28–35.
21. N. Nakada, T. Tsuchiyama, S. Takaki, and S. Hashizume: *ISIJ Int.*, 2007, vol. 47, pp. 1527–32.
22. T. Hara, N. Maruyama, Y. Shinohara, H. Asahi, G. Shigesato, M. Sugiyama, and T. Koseki: *ISIJ Int.*, 2009, vol. 49, pp. 1792–1800.
23. L. Liu, Z.-G. Yang, C. Zhang, and W.-B. Liu: *Mater. Sci. Eng., A*, 2010, vol. 527, pp. 7204–09.
24. L. Liu, Z.-G. Yang, and C. Zhang: *J. Alloy. Compd.*, 2013, vol. 577, pp. S654–S660.
25. F. Niessen, M. Villa, J. Hald, and M.A.J. Somers: *Mater. Des.*, 2017, vol. 116, pp. 8–15.

26. X. Zhang, G. Miyamoto, Y. Toji, S. Nambu, T. Koseki, and T. Furuhara: *Acta Mater.*, 2018, vol. 144, pp. 601–12.
27. Y. Zhang, C. Zhang, X. Yuan, D. Li, Y. Yin, and S. Li: *Materials*, 2019, vol. 12, p. 589.
28. A. Rosenauer, D. Brandl, G. Ressel, S. Lukas, C. Gruber, M. Stockinger, and R. Schnitzer: *Adv. Eng. Mater.*, 2023, vol. 25, p. 2300410.
29. N. Nakada, R. Fukagawa, T. Tsuchiyama, S. Takaki, D. Ponge, and D. Raabe: *ISIJ Int.*, 2013, vol. 53, pp. 1286–88.
30. N. Nakada, T. Tsuchiyama, S. Takaki, D. Ponge, and D. Raabe: *ISIJ Int.*, 2013, vol. 53, pp. 2275–77.
31. US-3178324-A: 1965.
32. Z. Nasiri, S. Ghaemifar, M. Naghizadeh, and H. Mirzadeh: *Met. Mater. Int.*, 2021, vol. 27, pp. 2078–94.
33. M. Taylor, Y.H. Mozumder, A.D. Smith, A.E. Davis, F. Scenini, P.B. Prangnell, and E.J. Pickering: *IOP Conf. Ser.: Mater. Sci. Eng.*, 2024, vol. 1310, p. 012001.
34. M. Taylor, J. Wang, Y.H. Mozumder, S.W. Williams, F. Scenini, P.B. Prangnell, and E.J. Pickering: *Metall. Mater. Trans. A*, 2025, https://doi.org/10.1007/s11661-025-07988-x.
35. Aerospace Material Specification AMS2759/2, 1984.
36. U.S. Patent and Trademark Office, US5681528A, 1997.
37. B.T. Daymond, N. Binot, M.L. Schmidt, S. Preston, R. Collins, and A. Shepherd: *J. Mater. Eng. Perform*, 2016, vol. 25, pp. 1539–53.
38. A.D. Smith, D. Lunt, M. Taylor, A. Davis, R. Thomas, F. Martinez, A. Candeias, A. Gholinia, M. Preuss, and J.M. Donoghue: *Ultramicroscopy*, 2025, vol. 280, p. 114244.
39. F. Bachmann, R. Hielscher, and H. Schaeben: *SSP*, 2010, vol. 160, pp. 63–68.
40. M. Taylor: 2025, All Data. https://doi.org/10.5281/zenodo.17288543.
41. F. Niessen, T. Nyyssönen, A.A. Gazder, and R. Hielscher: *J. Appl. Crystallogr.*, 2022, vol. 55, pp. 180–94.
42. R. Hielscher, T. Nyyssönen, F. Niessen, and A.A. Gazder: *Materialia*, 2022, vol. 22, p. 101399.
43. T. Nyyssönen, M. Isakov, P. Peura, and V.-T. Kuokkala: *Metall. Mater. Trans. A*, 2016, vol. 47A, pp. 2587–90.
44. G. Zhang, X. Yang, X. He, J. Li, and H. Hu: *Mater. Des.*, 2013, vol. 45, pp. 56–66.
45. W. Zheng, J. Zhu, and W. Yuan: *Mater. Charact.*, 2023, vol. 197, p. 112688.
46. M. Hunkel, H. Surm, and M. Steinbacher: *Handb. Therm. Anal. Calorim.*, 2018, vol. 6, pp. 103–29.
47. M. Taylor: 2025, Animated Gifs. https://doi.org/10.5281/zenodo.17288279.
48. T. Tsuchiyama, Y. Miyamoto, and S. Takaki: *ISIJ Int.*, 2001, vol. 41, pp. 1047–52.
49. T. Fu, L. Fu, D. Qin, C. Ye, S. Ma, M. Wen, and A. Shan: *Mater. Sci. Eng., A*, 2025, vol. 936, p. 148443.
50. G.Y. Lai, W.E. Wood, R.A. Clark, V.F. Zackay, and E.R. Parker: *Metall. Trans.*, 1974, vol. 5, pp. 1663–70.
51. R.O. Ritchie and R.M. Horn: *Metall. Trans. A*, 1978, vol. 9, pp. 331–41.
52. R. Padmanabhan and W.E. Wood: *Mater. Sci. Eng.*, 1984, vol. 66, pp. 1–11.
53. J. Luo, M.Q. Li, Y.G. Liu, and H.M. Sun: *Mater. Sci. Eng., A*, 2012, vol. 534, pp. 314–22.
54. G. Miyamoto, N. Iwata, N. Takayama, and T. Furuhara: *Acta Mater.*, 2010, vol. 58, pp. 6393–6403.
55. C. Ranger, V. Tari, S. Farjami, M.J. Merwin, L. Germain, and A. Rollett: *Metall. Mater. Trans. A*, 2018, vol. 49A, pp. 4521–35.
56. D. Sun, Z. Zhou, K. Zhang, X. Yang, X. Liu, Z. Guo, and J. Gu: *Mater. Des.*, 2023, vol. 227, p. 111692.
57. M. Taylor, A.D. Smith, J.M. Donoghue, T.L. Burnett, and E.J. Pickering: *Scripta Mater.*, 2024, vol. 242, p. 115924.
58. S.-J. Lee and Y.-K. Lee: *ISIJ Int.*, 2007, vol. 47, pp. 769–71.
59. J. Trzaska and L.A. Dobrzański: *J. Mater. Process. Technol.*, 2007, vol. 192–193, pp. 504–10.
60. J. Trzaska: *Arch. Metall. Mater.*, 2016, vol. 61, pp. 981–86.
61. M. Taylor, J.W. Fellowes, P.O. Hill, M.J. Rawson, T.L. Burnett, and E.J. Pickering: *IOP Conf. Ser.: Mater. Sci. Eng.*, 2022, vol. 1249, p. 012061.

Publisher's Note Springer Nature remains neutral with regard to jurisdictional claims in published maps and institutional affiliations.



https://dspace.org/

The effect of heating rate and hold time on grain refinement during the austenitisation of high-strength steels with coarse prior austenite grain structures

Taylor, Mark; Mozumder, Yahya H.; Smith, A. D.; Wang, Jun; Lu, Yao ...

2026-12-31
Springer
https://doi.org/10.1007/s11661-026-08241-9
Taylor M, Mozumder YH, Smith AD, et al., (2026) The Effect of Heating Rate and Hold Time on Grain Refinement During the Austenitisation of High-Strength Steels with Coarse Prior Austenite Grain Structures. Metallurgical and Materials Transactions A, Available online 25 may 2026

Downloaded from a DSpace repository. https://dspace.org/